[1]Portions reprinted, with permission, from C Coussot, S Kalyanam, R D Yapp and M F Insana, Fractional derivative models for ultrasonic characterization of polymer and breast tissue viscoelasticity, *IEEE Trans. Ultrason. Ferroelectr. Freq. Control*, in press, 2008 ©[2008 IEEE].

FRACTIONAL DERIVATIVE MODELS AND THEIR USE IN THE CHARACTERIZATION OF HYDROPOLYMER AND IN-VIVO BREAST TISSUE VISCOELASTICITY

BY

CECILE COUSSOT

B.S., Supelec, 2006

THESIS

Submitted in partial fulfillment of the requirements
for the degree of Master of Science in Bioengineering
in the Graduate College of the
University of Illinois at Urbana-Champaign, 2008

Urbana, Illinois

Adviser:

Professor Michael F. Insana

Abstract

The Viscoelastic response of hydropolymers, which include gelatin phantom and glandular breast tissue, may be accurately characterized with as few as three parameters using the Kelvin-Voigt Fractional Derivative (KVFD) modeling approach. We propose to image these parameters for simulated and experimental imaging phantoms and to estimate them for normal and cancerous in-vivo breast tissues. After a detailed presentation of the processing algorithm and discussion of its performances, we analyze the KVFD parameter values in simulated and experimental hydrogels. We show that the KVFD parameters can separate the biphasic mechanical properties of hydropolymers that describe the response of its solid and fluidic components and present the effects of pH and concentration changes in gelatin phantoms. We then interpret average results observed in normal and cancerous breast tissues and show that this modeling approach may be applied to tumor differentiation.

To my mother, always in my thoughts.

Acknowledgments

This project would not have been possible without the help of many people. Many thanks to my adviser, Michael Insana, for his encouragements and guidance. Thank you to Sureshkumar Kalyanam and to Rebecca Yapp for performing all those time-consuming simulations and experiments. Thanks to Yusuke Kawada for his assistance. Thanks to Mallika Sridhar and Karen Lindfors for their parts in the patient studies at UC Davis Medical Center. Thanks to the University of Illinois for awarding me a Carver Fellowship, providing me with the financial means to complete this project. Finally, thanks to Jean-Francois and to my family and friends for their constant support.

This material is based upon work supported by the NIH/NCI under Award No. R01CA082497.

Table of Contents

List of Tables . . . . . **vii**

List of Figures . . . . . **viii**

Chapter 1 Introduction **1**
1.1 Breast cancer development and detection 1
1.2 Elasticity imaging with ultrasound 2
1.3 Some previously presented rheological models 2
1.4 History of Fractional Derivatives 3

Chapter 2 Modeling relaxation and creep with Fractional Derivatives **5**
2.1 Power-law model of relaxation 5
2.2 Fractional Derivatives 8
2.3 KVFD models for relaxation and creep 10

Chapter 3 Imaging viscoelastic parameters α, E_0 and τ' **15**
3.1 Processing technique 15
3.1.1 Strain data acquisition 15
3.1.2 Processing technique 17
3.2 RF echo simulations with deformation 18
3.3 Gelatin imaging phantoms 20
3.3.1 Contrast from gelatin concentration 20
3.3.2 Contrast from pH 20

Chapter 4 Discussion of the algorithms performances **21**
4.1 Effects of changes in the data acquisition time 21
4.1.1 Influence on α 21
4.1.2 Influence on E_0 22
4.1.3 Influence on τ' 23
4.2 Effects of changes in the fitting frequency range 24
4.2.1 Influence on α 24
4.2.2 Influence on E_0 24
4.2.3 Influence on τ' 25
4.3 Global comparison of the two processing techniques 25

Chapter 5 Results **37**
5.1 Stiff inclusion image simulations 37
5.2 Gelatin phantoms 40
5.2.1 Higher concentration inclusion phantom 40
5.2.2 Acidic and basic inclusion phantoms 41
5.3 In-Vivo breast tissue data study 42
5.3.1 Average gelatin phantom and breast tissue responses 43
5.3.2 Cancer patient data 43

Chapter 6 Conclusion **50**

References **51**

Author's Biography **54**

List of Tables

5.1 FEA parameters values for two simulated phantoms 39
5.2 KVFD model parameter values for the object and ultrasonic strain sequences 40
5.3 KVFD model parameter values for an experimental gelatin phantom 41
5.4 Comparison of the KVFD model parameters in gelatin phantom and breast tissue . 43
5.5 KVFD model parameter values for in-vivo breast tissue data 44

List of Figures

2.1 Comparison of the numerical and modeled sum of exponentials according to time in the log-log space (where a power-decaying function is a straight line) for different values of a and τ_0. 9
2.2 Typical stress and strain step response of a Fractional-Derivative element. 11
2.3 Mechanical analogues to the polymer network and associated KVFD model. 12
2.4 Modeled strain versus time from Eq. (2.20) shown for different values of α and constants $E_0 = 1$ Pa and $\tau' = 10$ sec. 13

3.1 Illustration of the ultrasonic data acquisition and fit process. 16
3.2 Curve-fitting results on a simulated loss modulus. 18

4.1 Output vs input value of α given by the Fourier domain fit for different total acquisition times and levels of noise. 26
4.2 Output vs input value of α given by the time domain fit for different total acquisition times and levels of noise. 27
4.3 Output value of E_0 given by the Fourier domain fit vs input value of α for different total acquisition time and levels of noise. 28
4.4 Output value of E_0 given by the time domain fit vs input value of α for different total acquisition time and levels of noise. 29
4.5 Output value of τ' given by the Fourier domain fit vs input value of α for different acquisition times and levels of noise. 30
4.6 Output value of τ' given by the time domain fit vs input value of α for different acquisition times and levels of noise. 31
4.7 Output vs input value of α for different fitting frequency ranges and levels of noise. . 32
4.8 Output value of E_0 vs input value of α for different fitting frequency ranges and levels of noise. 33
4.9 Output value of τ' vs input value of α for different fitting frequency ranges and levels of noise. 34
4.10 Quality/price ratios for the Fourier and time domain processing algorithms according to the strain data acquisition time and sampling period. 35
4.11 Comparison of the Fourier and Time domain algorithms performances. 36

5.1 KVFD model images obtained for the strain image sequences generated from derivation of the interpolated FEA displacements: Object parametric images. 45
5.2 KVFD model images obtained for the strain image sequences generated from simulated echo data of two deformed FEA phantoms: Ultrasonic parametric images. . . . 46
5.3 KVFD parameter images for an experimental gelatin phantom with a stiff inclusion of diameter 8 mm. 47
5.4 Typical strain images obtained for two type-B gels respectively injected in the inclusion with an acidic and basic solution during polymerization and corresponding average KVFD parameter values in two regions. 48

5.5 Average creep response observed in an experimental phantom (a) and in breast tissue (b) fit in the time domain to Eq (2.20). 49

Chapter 1

Introduction

1.1 Breast cancer development and detection

Statistics from the American Cancer Society (ACS) show that breast cancer is the leading cancer type in women under 65. The ACS also indicated in 2007 that about 180,000 persons would be diagnosed with breast cancer while 41,000 patients would die. The last ten years have however seen a decrease of these numbers, which may be attributed to the improvement of diagnostic imaging and therapeutics.

Mammography and sonography are often the initial imaging techniques applied to patients when diagnosing breast tumors. Both modalities are considered able to better detect the presence of a lesion than to differentiate between benign and malignant tumors [1, 2]. For example, nearly all breast lesions appear as hypoechoic regions in sonograms; diagnosis requires careful visual evaluation of the lesion boundary, image texture and shadow features. To help improve discriminability, elasticity imaging was proposed because of its ability to reveal the presence of a stiff desmoplastic reaction specific to regions surrounding some malignant tumors [3]. Recent clinical experience examining the diagnostic performance of elasticity imaging for breast disease is very encouraging [4, 5, 6].

Static elasticity imaging techniques generate strain maps describing deformation patterns resulting from small, quasi-static, uniaxial compressions applied to the tissue surface as it is scanned ultrasonically. However, strain images are just the tip of the diagnostic information iceberg provided by mechanical properties. It is now known from molecular biology studies that cancerous epithelial cells must send and receive molecular signals to and from surrounding stromal cells if they are to develop into malignant tumors [7]. To effect malignant transformation, tumorigenic signaling pathways induce structural modifications to the extracellular matrix (ECM) and alter the viscosity of extracellular fluids, thus inducing changes to viscoelastic properties of the tissue. The most noticeable change is the palpable stiffening of breast stroma. Changes in the cellular mechanical environment can profoundly influence the progression of disease [8, 9]. Therefore time-varying features

of the viscoelastic (VE) response of breast tissues to gentle deforming forces may be an important untapped source of diagnostic information about both the biology of the malignant processes and the medicine of diagnosis and treatment monitoring.

1.2 Elasticity imaging with ultrasound

Elasticity imaging with ultrasound may be used to image small scale displacements of tissues in response to a stimulus. Radio-frequency (RF) echo signals from pulse-echo ultrasonic imaging systems are often used to image the strain response of tissues from applied stress stimuli [10]. Information about the VE properties of tissues is found from spatiotemporal variations in the corresponding strain fields. We form static strain images by processing ultrasonic RF echo frame sequences using a multi-resolution cross-correlation-based displacement algorithm [11] or a regularized optical-flow algorithm [12]; the algorithm choice depends on the amount of applied deformation. Both algorithms were designed to minimize strain noise for relatively large (>1%) deformations. Later generation algorithms [13, 14] provide superior strain estimates for the very small displacements (<0.1%) associated with radiation force stimuli [15] and viscoelastic creep imaging techniques [16]. For each volume element of tissue imaged, a time sequence of strain estimates is measured from which VE imaging parameters are extracted.

1.3 Some previously presented rheological models

Viscoelastic imaging parameters are selected from the parameters of rheological models applied to time-varying strain estimates. Model parameters summarize material properties of multiphasic polymeric media such as hydrogels and breast stroma. The best rheological models for our application yield just a few imaging parameters that are descriptive of the deformation physics and are also directly connected to the biology of disease. We found that a biphasic poroviscoelastic theory originally proposed by Mark [17, 18] and later modified by Suh and DiSilvestro [19] for articular cartilage could be adapted to reasonably represent the material behavior of hydrogels [16] and breast stroma [20]. The various components of the medium are grouped in two phases: a solid phase, consisting of a collagenous ECM with associated glycoproteins [21] and cells, and a fluid phase consisting of a viscous interfibrillar liquid. Gelatin hydrogels are structurally simpler than stromal tissues. Gels have a collagenous aggregate matrix of denatured type I collagen with electrically charged molecular side chains. The charged side chains act to "structure" nearby water molecules in a manner similar

to the function of glycoproteins in stroma. Thus the fluid viscosity varies depending on matrix density and structure.

In both tissues and gels, the solid matrix forms an ensemble of different size channels or "pores" through which fluid moves when the medium is loaded. However, the solid matrix itself behaves viscoelastically by virtue of the numerous hydrogen-bonded cross links between matrix fibers. The strain response of a hydropolymer medium subjected to a step stress (creep experiment) has been described by a generalized Kelvin-Voigt model consisting of the sum of many real exponential functions [22, 16]. While such a model is easily adaptable to random pore sizes and variations matrix cross-link strength, it requires at least two parameters for each Voigt unit to fully represent the mechanical response. The dimensionality of this straightforward model is very large.

We described a method for reducing the dimensionality of the generalized Kelvin-Voigt model by applying singular-value decomposition methods [23]. Imaging parameters were selected from the largest eigenvalues of the creep curve and hence represented the dominant features of the polymer response. Because the compliance loss spectrum from breast stroma [20] and hydrogels [16] classifies these media as amorphous, weakly cross-linked polymers with distinct solid and fluid spectral responses [22], a two component Kelvin-Voigt model was proposed. Parameters were then associated with the two phases. However, spectral separability of the phases depends significantly on boundary conditions. For the unconfined, uniaxial compressions usually applied in static strain imaging techniques, overlap of the bimodal response was often observed. Clearly, we need a rheological model that considers the continuous nature of mechanisms governing the slow relaxation of polymers. In experimental situations where no clearly dominant mechanistic components emerge from creep data, the rheological model should provide a concise set of model parameters for imaging.

1.4 History of Fractional Derivatives

In the last few decades, several papers have been devoted to the definition of concise models involving fractional calculus approaches that would represent this complex VE response while retaining diagnostic contrast and physical interpretation [24, 25, 26, 27, 28]. Indeed, because the Fractional Derivative (FD) of a function depends on its whole time history, and not on its instantaneous behavior, they are perfectly suited for the description of materials with memory, such as polymers or tissues.

Viscoelastic models based on fractional derivatives (FD) were introduced by Sloninsky in 1967

[29] to find a parsimonious representation for complex media. The mechanical responses predicted by such models were found to be consistent with Rouse's molecular theory of polymers by Bagley and Torvik [24]. Schiessel and Blumen [30] derived hierarchical mechanical analogs to fractional derivative elements and models by assembling numerous springs and dashpots (elastic and viscous terms, respectively) in series and parallel. FD models of increasing complexity were proposed [27] to model the rheological behavior of synthetic polymers as well as biological cells and tissues [26, 28, 31]. Indeed, because the fractional derivative of a function depends on its whole time history and not on its instantaneous behavior, they are perfectly suited for the description of materials with memory, such as polymers or tissues. Originally, FD models appeared as purely phenomenological models, but others recently contributed statistical, physical, and mathematical justifications for FD applications [32, 33, 34]. My first goal in this thesis is to review the extensive literature on Kelvin-Voigt fractional derivative (KVFD) rheological models for the study of hydropolymers mechanical behavior and develop imaging methods that can be interpreted in terms of the biphasic properties.

Previous studies related to fractional derivative rheological models often consisted of blindly fitting FD models to the viscoelastic responses of various materials without either justifying the use of such model or analyzing the physical meaning of the results. On the contrary, we begin here by reviewing how fractional derivatives arise naturally from slowly varying distributions of exponential relaxations (Kelvin Voigt units) in the VE response. We then apply a three-parameter KVFD model to represent the dynamic behaviors of hydrogels and in-vivo breast tissues. Images of the corresponding FD parameters for simulated hydropolymers, experimental phantoms and in-vivo breast tissues are generated and interpreted in terms of the stiffness and fluidity of the material.

Chapter 2

Modeling relaxation and creep with Fractional Derivatives

2.1 Power-law model of relaxation

In a stress-relaxation experiment, the force response of a sample to a known applied deformation is measured versus time. The FD model assumes that the polymer network undergoing viscoelastic relaxation can be modeled by the linear superposition of many elementary viscoelastic (Maxwell) units. The incremental change in stress for the n-th viscoelastic element as a function of time, $d\sigma_n(t)$, increases in proportion to the incremental change in strain, $d\epsilon_n(t)$, and decreases in proportion to the time increment according to the equations

$$d\sigma_n(t) = E'_n d\epsilon_n(t) - \frac{E'_n}{\eta_n}\sigma_n(t)dt$$

$$\text{or} \quad \dot{\sigma}_n(t) = E'_n \dot{\epsilon}_n(t) - \frac{1}{\tau_n}\sigma_n(t) \ \text{ where } \ \dot{\sigma}_n(t) = \frac{d\sigma_n}{dt} \ . \tag{2.1}$$

E'_n and η_n are, respectively, the elastic modulus and viscous coefficients and $\tau_n = \eta_n/E'_n$ is the viscoelastic time constant for the unit. The first term on the right side of Eq. 2.1 is the elastic stress response and the second term is the viscoelastic stress response.

Taking the one-sided Laplace transform of Eq. 2.1 and solving for stress, we find

$$\tilde{\sigma}_n(s) = \frac{E'_n \tau_n}{1+\tau_n s} s\tilde{\epsilon}_n(s) \ . \tag{2.2}$$

Finally, applying the convolution theorem to find the inverse Laplace transform of Eq. 2.2, we obtain

$$\sigma_n(t) = \int_0^t dt' \, E_n(t-t') \, \dot{\epsilon}_n(t') \ , \tag{2.3}$$

where we assume each Maxwell unit is linear, time-invariant, and initially at rest. The modulus $E_n(t)$ describes material properties of the n-th polymer component through two constants, E'_n and

τ_n, via

$$E_n(t) = E'_n \; e^{-t/\tau_n} \; .$$

The relaxation modulus for the polymer is the sum of contributions from all N units [34],

$$E(t) = \sum_{n=0}^{N} E'_n \; e^{-t/\tau_n} \; , \tag{2.4}$$

where unit constants are assumed to vary slowly with n. This interdependency can be modeled recursively with two scaling parameters a and b:

$$E'_n = bE'_{n-1} = b^n E'_0 \tag{2.5}$$

$$\tau_n = \frac{\tau_{n-1}}{a} = \frac{\tau_0}{a^n} \tag{2.6}$$

Combining Eqs (2.4) – (2.6) we obtain

$$\begin{aligned} E(t) &= E'_0 \sum_{n=0}^{N} b^n e^{-a^n t/\tau_0} \\ &= E'_0 \sum_{n=0}^{N} e^{F(n,t)} \; , \end{aligned} \tag{2.7}$$

where $F(n,t) = n \ln b - a^n t/\tau_0$.

It is observed with polymers that the time dependence of the elastic modulus $E(t)$ is a power law. Let n_0 indicate the viscoelastic unit where $e^{F(n_0,t)}$ is maximum and let us assume that the material constants E'_n and τ_n from sequential units vary slowly and monotonically. Consequently the unit responses are highly correlated, and $F(n,t)$ is well represented by a second-order Taylor series expansion about n_0.

$$F(n,t) \simeq F(n_0,t) \; + \; \frac{(n-n_0)^2}{2} \left(\frac{\partial^2 F}{\partial n^2} \right)_{n_0} \; , \tag{2.8}$$

since $(\frac{\partial F}{\partial n})_{n_0} = 0$. Combining the definition of $F(n,t)$ in Eq (2.7) with its first derivative being zero, we find that

$$n_0 = \frac{\ln(\alpha\tau_0) - \ln t}{\ln a} \quad \text{where} \;\; \alpha = \frac{\ln b}{\ln a} \; . \tag{2.9}$$

We restrict the range of acceptable model constants a and b to those producing physical models of elastic moduli with power-law form. Realistic models require $\tau_n > 0$ for all n; therefore Eq (2.6)

gives $a > 0$. E'_n must be positive and remain finite, consequently $0 < b < 1$. In order for $e^{F(n_0,t)}$ to exist and be a maximum for all t, E'_n and τ_n must vary in opposite ways. For example, experiments show that $E(t)$ decreases with time. If E'_n decrease with n, then τ_n must increase with n to obtain a power-law form. From this relation, we can derive that $0 < a < 1$. These bounds on model constants have been experimentally verified [35]. The power-law assumption also does not permit a to approach 1; that is, from Eq (2.7),

$$\lim_{a\to 1, N\to\infty} E(t) = \frac{E'_0}{1-b}\, e^{-t/\tau_0}$$

is a pure exponential. Regardless, we note that α is defined for the range of constants $0 < b, a < 1$.

We now posit that a continuum of viscoelastic units contributes to the elastic modulus, $E(t)$. Therefore $N \to \infty$. A continuum model is consistent with the hypothesis that the viscoelastic response of the collagen matrix results from relaxation of hydrogen bonds having a continuous spectrum of bond strengths [22]. Combining Eqs (2.7) – (2.9), we follow Kawada [34] to obtain the power-law form,

$$\begin{aligned}
E(t) &\simeq E'_0 \sum_{n=0}^{\infty} e^{F(n_0,t)+\frac{(n-n_0)^2}{2}\left(\frac{\partial^2 F}{\partial n^2}\right)_{n_0}} \\
&= E'_0 \sum_{n=0}^{N} e^{\alpha(\ln(\alpha\tau_0)-\ln(t)-1)-\frac{(n-n_0)^2}{2}\alpha(\ln a)^2} \\
&= E'_0\, e^{\alpha(\ln(\alpha\tau_0)-1)} t^{-\alpha} \sum_{n=0}^{N} e^{-\alpha(\ln a)^2\frac{(n-n_0)^2}{2}} \\
&\simeq E'_0\, e^{\alpha(\ln(\alpha\tau_0)-1)} \sqrt{\frac{2\pi}{\ln a\, \ln b}}\; t^{-\alpha} \\
&\simeq \Phi\, t^{-\alpha}\,, \qquad (2.10)
\end{aligned}$$

where all time-independent factors are collected into Φ. On a log-log scale, $E(t)$ is a straight line with slope $-\alpha$ and intercept $\ln\Phi$. Applying unitless parameters, we find the alternative form

$$\frac{E(t)}{E_1} = \frac{1}{\Gamma(1-\alpha)}\left(\frac{t}{\tau}\right)^{-\alpha}\,, \qquad (2.11)$$

where E_1 is the scaled modulus for unit n_0, τ is a characteristic relaxation time constant, and Γ is the Gamma function for non-integer arguments.

We numerically summed the decaying responses of 1000 exponentials for $E'_0 = 1$ and various values of a, b and τ_0. We compared them to the corresponding analytical models defined by Eq.

(2.11) and obtained the results displayed in Fig. 2.1. As pointed out earlier, the data do not follow the model in cases where a is too close to 1, which corresponds to all the exponentials having very similar characteristic times. In the same way, the model disagrees with the numerical sum when τ_0 is too large compared to the observation time. Indeed, the time constants, as defined by our model, can only increase. When τ_0 is too large, the behavior of the sum, at short times, is given by the initial exponential. These limitations are however of little interest since they are related to the definition of the model, and not to real data. Indeed, for real experiments, the time constants can generally be assumed as widespread and the model holds, as can be seen in Fig. 2.1.c.

2.2 Fractional Derivatives

Power-law viscoelastic responses suggest properties of self-similarity and memory, which are the features described by fractional derivatives. The Riemann-Liouville definition of a fractional derivative operator applied to function f is

$$ {}_a\mathcal{D}_t^{-\gamma}(f) \triangleq \frac{1}{\Gamma(\gamma)} \int_a^t dt' f(t')(t-t')^{\gamma-1} \, . \tag{2.12} $$

Combining Eqs (2.3), (2.11) and (2.12), the net constitutive equation may be written as

$$ \begin{aligned} \sigma(t) &= \frac{E_1\tau^\alpha}{\Gamma(1-\alpha)} \int_0^t dt'(t-t')^{-\alpha} \, \frac{d\epsilon(t')}{dt'} \\ &= \frac{E_1\tau^\alpha}{\Gamma(\gamma)} \int_0^t dt'(t-t')^{\gamma-1} \frac{d\epsilon(t')}{dt'} \quad \text{for } \gamma = 1-\alpha \\ &= E_1\tau^\alpha \, {}_0\mathcal{D}_t^{-\gamma} \left(\frac{d\epsilon(t)}{dt} \right) \quad \text{by definition of } {}_a\mathcal{D}_t^{-\gamma}(f) \\ &= E_1\tau^\alpha \, {}_0\mathcal{D}_t^{\alpha-1} \left(\frac{d\epsilon(t)}{dt} \right) \\ &= E_1\tau^\alpha \, \frac{d^{\alpha-1}}{dt^{\alpha-1}} \left(\frac{d\epsilon(t)}{dt} \right) \\ \sigma(t) &= E_1\tau^\alpha \, \frac{d^\alpha \epsilon}{dt^\alpha} \end{aligned} \tag{2.13} $$

Eq (2.13) is more intuitive when expressed in the radial frequency domain, ω. Applying the Fourier derivative theorem we find

$$ \sigma(\omega) = E_1\tau^\alpha (i\omega)^\alpha \epsilon(\omega) \, , \tag{2.14} $$

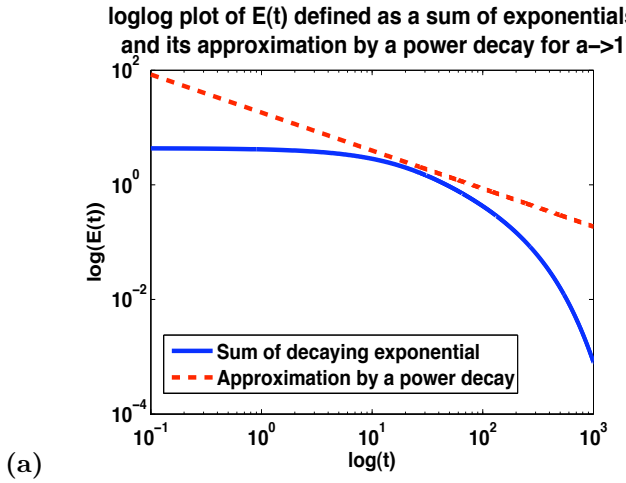

(a)

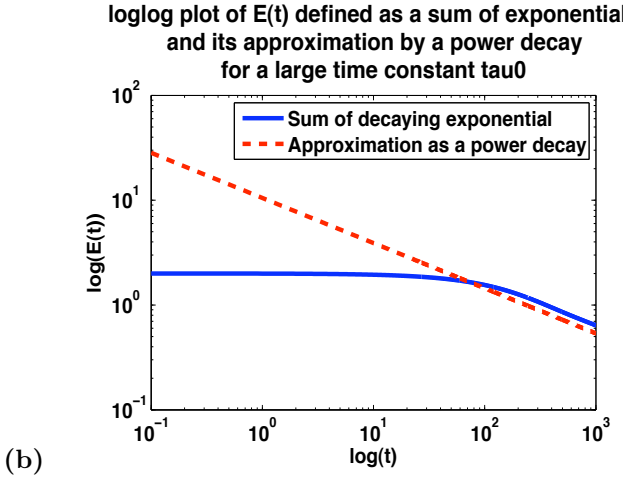

(b)

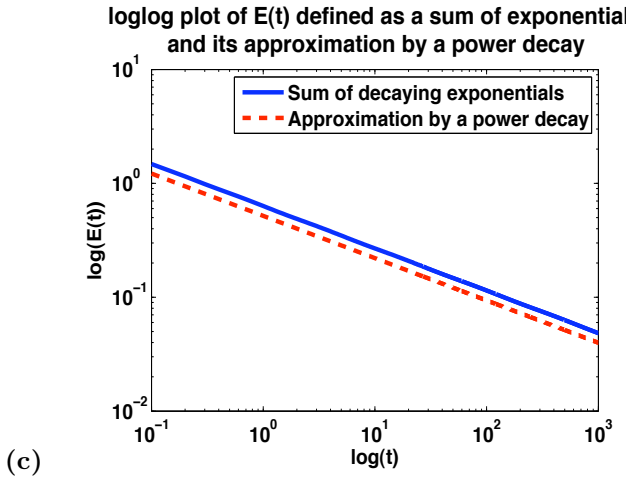

(c)

Figure 2.1: Comparison of the numerical and modeled sum of exponentials according to time in the log-log space (where a power-decaying function is a straight line) for different values of a and τ_0. In a) is shown the sum of exponentials and its approximation by a power decay when $a \to 1$. As stated previously in that case, the sum of exponentials remains an exponential and the approximation is false. In b), τ_0 is one fifth of the whole observation time, which is too long to approximate the sum by a power decay at low times where one exponential clearly dominates. Finally, a more general case is displayed in c) for $a = 0.2$, $b = 0.55$ and $\tau_0 <<$ observation time. An offset, most likely due to the approximation of the constant in Eq 2.10, appears, but the slopes of both curves are similar, which shows that a large sum of exponentials may be modeled by a power-decaying function.

from which the complex modulus is defined as

$$E^*(\omega) \triangleq \frac{\sigma(\omega)}{\epsilon(\omega)} = E_1(i\omega\tau)^\alpha \ , \tag{2.15}$$

and the complex compliance as

$$D^*(\omega) \triangleq \frac{\epsilon(\omega)}{\sigma(\omega)} = \left[(i\omega\tau)^\alpha \ E_1\right]^{-1} \ . \tag{2.16}$$

Eqs (2.15) defines FD units referred to as "spring-pots" because of their ability to combine large assemblies of Maxwell or Voigt (exponential) units to predict non-exponential relaxation and creep behavior, respectively. Advantages of this model include just three parameters, α, τ, and E_1, and a straightforward physical interpretation. When $\alpha \to 0$ the fractional unit behaves like a Hookean spring, when $\alpha \to 1$ it behaves as a Newtonian dashpot. For intermediate values of α, it behaves as a viscoelastic material. Though a spring-pot could be modeled by a hierarchical assembly of springs and dashpots [30], our goal here is to keep a concise feature space. However, a spring-pot alone cannot model the relaxation and creep responses typically observed in polymers, which can plateau over time, and thus the model must be expanded further.

2.3 KVFD models for relaxation and creep

As illustrated in Fig. 2.2, a spring-pot alone cannot model a physical behavior. Adding a spring in parallel with the spring-pot unit (see Fig. 2.3) however allows for the relaxation plateau observed experimentally. This is the Kelvin-Voigt Fractional Derivative (KVFD) model given by,

$$\sigma(t) = E_0\epsilon(t) + E_1\tau^\alpha \frac{d^\alpha \epsilon(t)}{dt^\alpha} \ , \tag{2.17}$$

and consisting of elastic and viscoelastic terms. E_0 and E_1 may have different values, however we can define τ' such that $\tau' = \left(\frac{E_1}{E_0}\right)^\alpha \tau$ which transforms the previous equation into

$$\sigma(t) = E_0\epsilon(t) + E_0\tau'^\alpha \frac{d^\alpha \epsilon(t)}{dt^\alpha} \ . \tag{2.18}$$

This form is convenient when expressing the time domain behavior in response to a step stimulus.

Considering stress-relaxation data, where a uniaxial compressive step strain is applied to a sam-

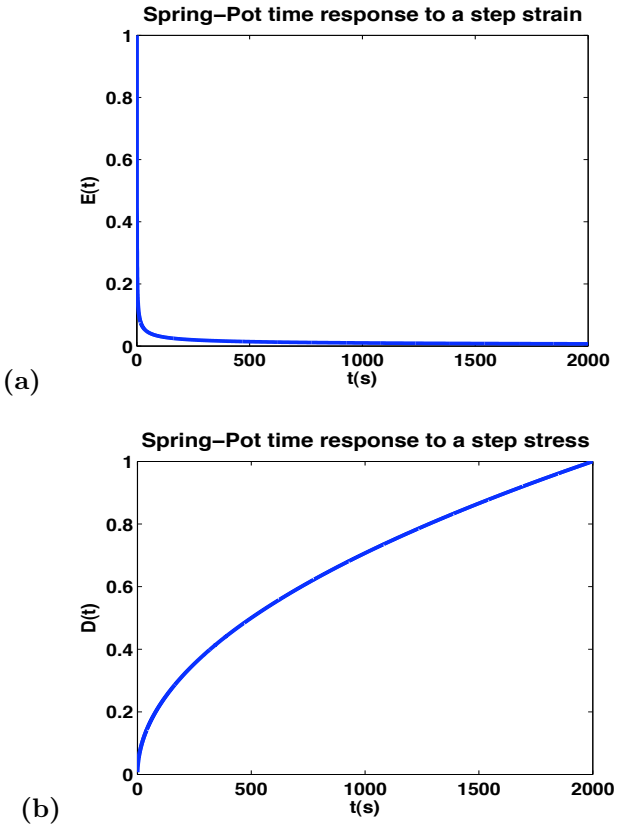

Figure 2.2: Typical stress and strain step response of a Fractional-Derivative element. In (a), a typical normalized stress response to a step strain is given. Notice that as time increases, the material's stress tends to 0. In (b), a typical normalized strain response to a step stress is given. Notice that in this case, the material keeps responding to the stress and rearranging. Both responses are non-physical.

ple, we have $\dot{\epsilon}(t) = \epsilon_0 \delta(t)$ and from Eq (2.18)

$$\frac{\sigma(t)}{\epsilon_0} = E(t) = E_0 + \frac{E_0}{\Gamma(1-\alpha)} \left(\frac{t}{\tau'}\right)^{-\alpha} . \tag{2.19}$$

Because we measure strain ultrasonically and not stress, we usually conduct creep experiments to image viscoelastic properties. In these experiments, a constant step stress is applied to the sample. Schiessel et al. [36] showed that the compliance expression for the KVFD model corresponding to the modulus expression in Eq (2.19) is

$$\frac{\epsilon(t)}{\sigma_0} = D(t) = \frac{1}{E_0} \left(\frac{t}{\tau'}\right)^{\alpha} \boldsymbol{E}_{\alpha,1+\alpha} \left(-\left(\frac{t}{\tau'}\right)^{\alpha}\right) \tag{2.20}$$

where $\boldsymbol{E}$ is a type of hypergeometric function known as the generalized Mittag-Leffler function [37]

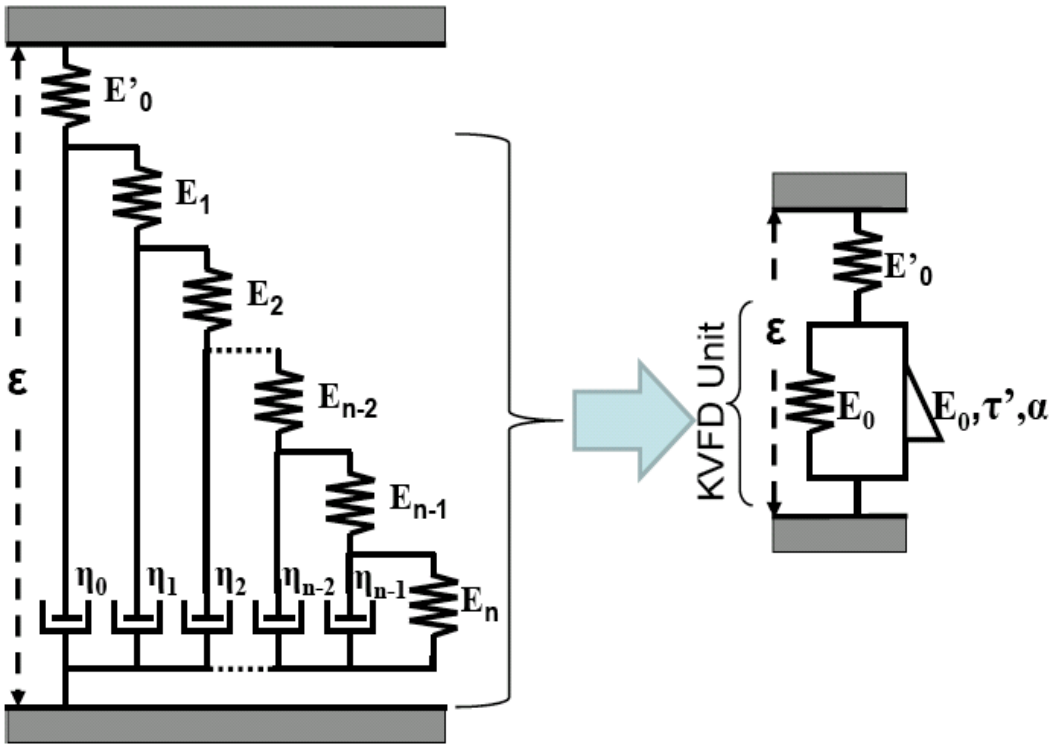

Figure 2.3: Mechanical analogues to the polymer network and associated KVFD model. Though any material could be modeled as an assembly of springs and dashpots in series and parallel as presented in [36] and shown here, our goal is to keep as few parameters as possible, which is achieved by the use of the KVFD unit (on the right) in which the spring-pot is represented as a triangle.

and defined by:

$$\boldsymbol{E}_{\alpha,\beta}(z) = \sum_{k=0}^{\infty} \frac{z^k}{\Gamma(\alpha k + \beta)} \quad \text{for } \alpha, \beta > 0 \, . \tag{2.21}$$

Figure 2.4 displays the modeled time behavior of compliance according to Eq. (2.20) for values of α from 0.2 to 0.8 in steps of 0.2. Lower values of α induce quick responses of low amplitude while higher values are responsible for slower reactions exhibiting greater net strain. These two types of behavior respectively describe more elastic and more viscous materials.

The more complex expression for compliance in the time domain, as compared with relaxation, is a consequence of the following relation between $D(t)$ and $E(t)$ [38]:

$$\int_{-\infty}^{t} E(t - t')D(t')dt' = t \, . \tag{2.22}$$

Computation is simplified by transforming Eq. (2.18) into the Fourier domain resulting in the

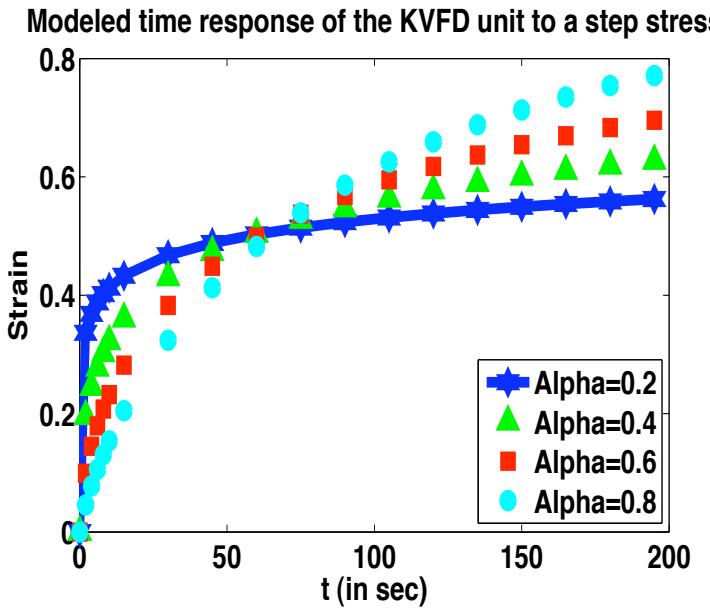

Figure 2.4: Modeled strain versus time from Eq. (2.20) shown for different values of α and constants $E_0 = 1$ Pa and $\tau' = 10$ sec. A unit step stress is assumed so $D(t) = \epsilon(t)$. When α is low, the maximum amplitude of the creep is lower but the material strains faster, which is typical of stiff or elastic media. On the opposite, a high α causes a slower response of larger amplitude, which is typical of more viscous materials.

following expression of the complex modulus

$$\begin{aligned} E^*(\omega) &= E_0 + (i\omega\tau')^\alpha E_0 \\ &= E_0\left(1 + (e^{i\pi/2}\omega\tau')^\alpha\right) \\ &= \left(E_0 + E_0\tau'^\alpha \cos\left(\frac{\pi\alpha}{2}\right)\omega^\alpha\right) + iE_0\tau'^\alpha \sin\left(\frac{\pi\alpha}{2}\right)\omega^\alpha \ . \end{aligned} \tag{2.23}$$

The loss modulus, which describes the deformation energy dissipated as heat, is given by the imaginary part of the complex modulus:

$$\begin{aligned} \Im E^*(\omega) &\triangleq E''(\omega) \\ &= (\omega\tau')^\alpha E_0 \sin\left(\frac{\alpha\pi}{2}\right) \ . \end{aligned} \tag{2.24}$$

Plotting $\ln E''(\omega)$ versus $\ln\omega$, we find a linear function with positive slope α. Curve fitting is therefore significantly faster in the frequency domain than in the time domain.

As stated earlier, strain and not stress is measured experimentally. Hence, the loss modulus

$E''(\omega)$ must be derived from the compliance using

$$\begin{aligned} E''(\omega) &= \Im E^*(\omega) \\ &= \Im \frac{1}{D^*(\omega)} \, . \end{aligned} \tag{2.25}$$

It must also be noted that the KVFD unit only characterizes part of the polymers' response to a step stress. The viscoelastic response of polymers can be seen as the superposition of 3 elements [16]: a purely elastic initial response, accounted by a spring associated to the KVFD unit in series as shown in Fig. 2.3 and which we do not study here, a viscoelastic response, modeled here by the KVFD unit, and a flow element (responsible for a linearly increasing slope when $t \to \infty$). Here, the initial elastic response and flow terms are removed in order to focus on the KVFD unit response. The viscoelastic response of the material is then modeled with as few as three parameters. By imaging the values of α, E_0 and τ' for hydropolymers or in-vivo tissues, we intend to display with only a few frames their relevant viscoelastic characteristics.

Chapter 3

Imaging viscoelastic parameters α, E_0 and τ'

3.1 Processing technique

3.1.1 Strain data acquisition

Ultrasonic data were acquired to estimate viscoelastic parameters during creep experiments as illustrated in Fig. 3.1. A linear array transducer was used to apply a step force at the top surface and maintain it constant while ultrasonic RF echo frames were recorded. A Siemens Sonoline-Antares system with an ultrasonic research interface was used for all experiments. A VF10-5 linear array transducer transmitted broadband 8 MHz pulses. Echo frames are recorded beginning immediately prior to the application of a 1 s ramp load ($\sim 4N$) at rates between 1 and 4 fps for up to 2000 s. The frame rate was set on the Antares system by a waveform generator that triggered the ECG module on the scanner. Because scanner memory was limited, there is a few-seconds gap between groups of 60-100 RF frames as memory contents were downloaded to disk. For clinical breast scanning the frame rate was fixed at 13 fps for a 10-20 s acquisition time. The frame rate for RF echo simulations (described below) was adjusted between 0.01 and 10 fps as required by the material parameters selected for the finite element analysis (FEA) to properly sample the creep curves. Sampling issues and deconvolution of the strain series to estimate compliance spectra were detailed in [20].

A time series of strain images was formed from the RF echo frames off line by applying a multi-resolution cross-correlation strain algorithm [11]. For each pixel in the spatially-registered strain image series pictured in Fig. 3.1, we plotted the computed strain values versus time to obtain a creep curve. As described previously [23], we applied a preprocessing step to the strain data that eliminates purely elastic and purely viscous effects, thus isolating the viscoelastic creep response, e.g., Eq (2.20). Applying Eqs (2.19), (2.24) to creep curves, we used Fourier methods to estimate the viscoelastic parameters for all data except the in vivo breast data. The frequency range in the loss spectrum plotted on log-log axes that exhibits a linear response was selected for analysis.

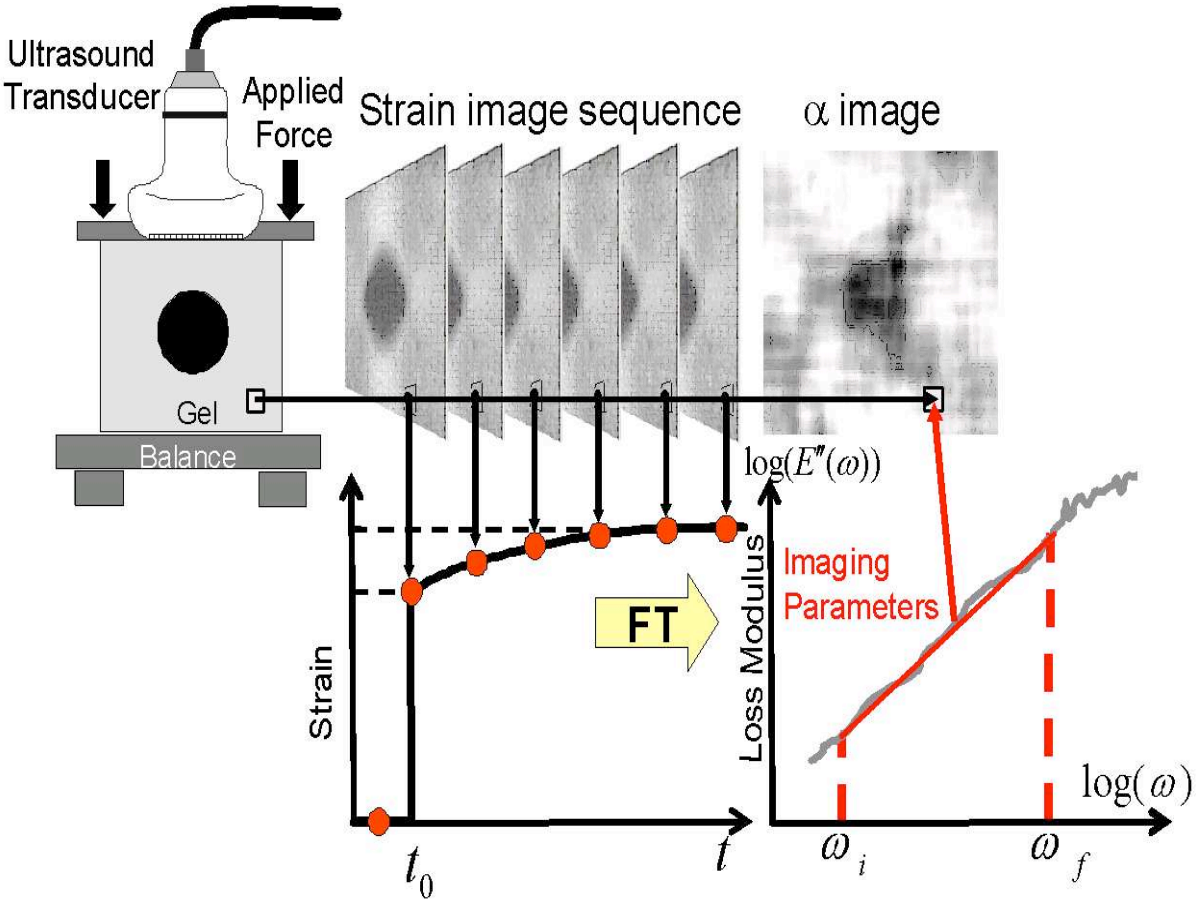

Figure 3.1: Illustration of the ultrasonic data acquisition and fit process. From a time series of RF echo frames, a time series of strain images are formed and processed to generate KVFD model parameter images, among which the α image.

3.1.2 Processing technique

The equations in chapter 2 show that the viscoelastic parameters E_0, τ' and α may be estimated in the frequency domain from either the loss modulus $E''(\omega)$ or the loss compliance $D''(\omega)$ depending on whether stress relaxation or creep experiments are employed. Estimates can be obtained directly from time domain data at considerably greater computational cost. Time-domain processing is preferred for short duration strain acquisitions (in vivo breast data) because of lower noise and parameter estimation uncertainty.

In the Fourier domain, the estimated values of the three parameters of the KVFD model obtained from the fit are however correlated. As stated earlier, a linear fit may be performed in the log-log domain over a user-defined frequency range on the loss modulus. This fit provides an estimate for α and $ln(\tau'^{\alpha} E_0 \sin\left(\frac{\alpha\pi}{2}\right))$. The remaining necessary information to approximate the three unknowns is extracted from the time domain strain curve using $\frac{\sigma_0}{\epsilon_\infty} \approx E_0$. If the acquisition time is long enough, this value can be estimated and a third equation is obtained, which allows us to estimate the KVFD parameters from a simple linear fit. This once again justifies the need for long acquisition times when processing data in the Fourier domain.

Strain curves may be directly fitted to Eq (2.20) to estimate the model parameters in the time domain. In that case, the fitting is non linear and leads to a unique solution but requires a significantly higher processing time. In order to limit it, the algorithm is initialized at the values obtained from the Fourier domain processing. Because of its computational cost, the time domain fitting is generally limited to small data sets, and cannot typically be used to obtain parameter images. We therefore focus this chapter on the Fourier domain processing of the data and on the two most important fitting parameters.

The first critical parameter is the frequency range over which the fit is performed. When representing the loss modulus in the log-log space, a straight line appears and the model clearly fits over part of the bandwidth. It was however pointed out in [26] that the KVFD model doesn't hold at high frequencies (typically above 10^2 rad.s^{-1}). Moreover, a high frequency processing noise interfered considerably with our experimental data, as can be seen in Fig. 3.2. We therefore limited the fitting area to the frequency range over which the noise is minimum and the loss modulus linear in the log-log space, i.e. [0.03 to 0.3] rad.s^{-1} for simulation data, and to [0.1 to 0.6] rad.s^{-1} for experimental phantom or tissue data.

Parametric noise was reduced by averaging creep curves from a local neighborhood of strain pixels before parameter estimation. Hence, another critical element is the size of this spatially

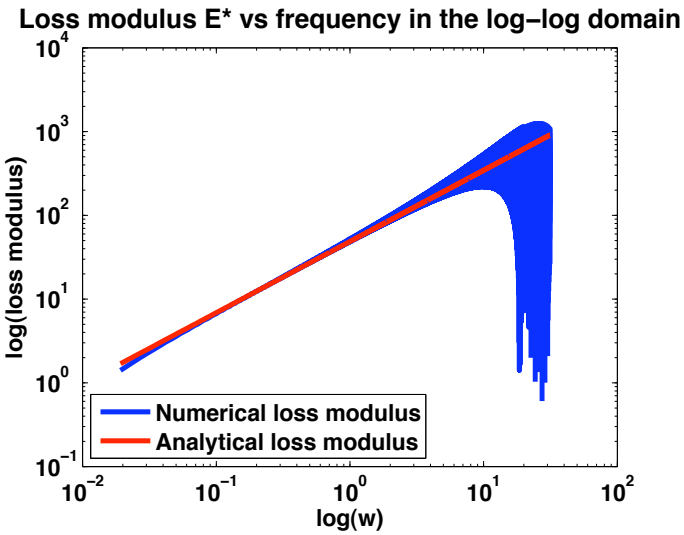

Figure 3.2: Curve-fitting results on a simulated loss modulus. At very low and very high frequency, we observe processing noise. However, in the frequency range we typically use for real data, we obtain a relatively good fit of the analytical model to the processed data. The modeled parameters are $\alpha = 0.85$, $\tau' = 100$ s and $E_0 = 1$ Pa, and the sampling period 0.1 s.

averaging window which is correlated to the size of the companding window used to compute the strain. A companding window of 256 pixels leads to smoother strain curves than windows of 64 pixels only, but strain images obtained via the former have also lost spatial resolution and further spatial averaging is limited. Thus, spatial averaging reduces image noise at the cost of parametric spatial resolution. An example of an α image using a 27×49 pixels spatial averaging window is shown in Fig. 3.1, top right.

The viscoelastic part of the strain curve is then transformed to the frequency domain in order for the loss modulus to be fit to Eq. (2.24) with a least-squares algorithm in a user-defined frequency range. This range depends on the noise level of the loss modulus and on the acquisition time. The fitting parameters are then assigned to the center pixel of the window and images of $\alpha(x, y)$, $E_0(x, y)$ and $\tau'(x, y)$ are obtained.

3.2 RF echo simulations with deformation

We simulated ultrasonic RF echo signals from uniformly scattering media with spatially varying viscoelastic properties. The goal was to discover how spatial variations in material properties influence spatial variations in estimates of E_0, τ', and α.

2-D random scattering fields were generated in Matlab® to facilitate simulation of RF echo frames with fully-developed speckle such as those from uniform graphite-gelatin phantoms [16]. The

scattering field was numerically generated so that the coordinate of each scatterer was preserved as a floating-point value. Corresponding to the scattering field was a meshed map of viscoelastic material properties that was used in a Finite Element Analysis. Displacements from the FEA output were used to reposition each scatterer in the scattering field to simulate continuous spatial deformation. The resulting scattering field was convolved with an ultrasonic pulse-echo impulse response typical of the Siemens Antares system data. Details of the RF echo simulations are provided elsewhere [39].

ABAQUS® commercial FEA software was used to simulate deformations of the scatterer field. The software allows the modeling of a biphasic poroviscoelastic medium with spatial heterogeneities in which the strain response to a load is determined by a viscoelastic solid matrix and fluid flow through the porous solid matrix. The viscoelastic nature of the solid matrix phase is specified using the relaxation constants of the discrete shear relaxation spectrum g_1 and g_2 and associated time constants τ_1 and τ_2. The normalized shear modulus of the matrix is modeled as

$$g(t) = \frac{G(t)}{G_0} = 1 + g_1 e^{-t/\tau_1} + g_2 e^{-t/\tau_2} \ .$$

Other FEA model parameters are the elastic modulus, E_m, and Poisson's ratio, ν_m, of the porous solid matrix phase. Finally, the fluid-flow-dependant viscoelastic behavior is specified by the hydraulic permeability, k, of the fluid movement through the porous matrix.

We simulated echo data from the central axial plane of a cylindrical phantom assuming axisymmetric deformation. The meshed field included an 8-node plane strain porous element (CPE8P) in ABAQUS. A uniform compressive stress of 100 Pa was applied to the top surface, the side surfaces were unbounded and the bottom surface permitted no vertical displacement. Top and bottom surfaces were traction-free. The medium contained a circular inclusion that varied only in mechanical properties from its background. The material property values of the background and inclusion for two FEA simulations are given in Table 5.1. Derivatives of the interpolated FEA displacements provided us with ideal time series of strain images, referred to here as object strain frames, while RF echo data were generated by displacing scatterers according to the FEA and processed with the MRCC algorithm in order to obtain strain frames sequences, referred to as ultrasonic strain frames.

3.3 Gelatin imaging phantoms

3.3.1 Contrast from gelatin concentration

A 5-cm cubic graphite-in-gelatin phantom block containing a stiff cylindrical inclusion was imaged in this study [23]. This phantom contained a 5.5% background concentration by weight of type-A animal-hide gelatin. Embedded within the block was an 8-mm-dia inclusion with a concentration of 8% gelatin. Throughout the phantom, graphite powder (3% concentration by weight) was added to generate ultrasonically tissue-like scattering and absorption. Also 0.1% by volume formaldehyde was added as a chemical cross linker. The balance of the phantom material was distilled water. Although the inclusion provided little ultrasonic contrast, it generated contrast in viscoelastic features. The higher gelatin concentration of the inclusion created a stiffer more solid polymer that relaxed slower than its background.

3.3.2 Contrast from pH

Two additional 5-cm graphite-in-gelatin blocks were constructed. Both were made of 8% type-B gelatin throughout. However, during gelation, a linear track of acidic fluid was injected in one block and a basic fluid track in the other. Acids or basis applied during gelation have been shown to weaken the polymer structure by causing a charge imbalance during polymerization, which respectively causes a softening or stiffening of the material. With these phantoms, we expect to see little ultrasonic contrast and significant viscoelastic contrast from the fluid injection sites. The goal is to use α images to see how pH affects the liquid-solid components of the hydrogel. pH effects are thought to play an important role in the elasticity image contrast of cancer.

Chapter 4

Discussion of the algorithms performances

We previously presented two fitting algorithms: One involving a time domain fit of the material's strain curves, and one performing the fit on the loss modulus in the Fourier domain. In order to present clearly the advantages and drawbacks of each technique depending on the main characteristics of the data, we performed several simulations and observed the effects of changes in the data set characteristics and processing parameters. The results of these simulations are discussed here.

4.1 Effects of changes in the data acquisition time

For this section, we generated creep curves according to Eq. (2.20). The values of E_0 and τ' were fixed, respectively, at 10 Pa and 2 s and the data sampling rate was 10Hz. Curves were generated for values of α going from 0.1 to 0.9 by an 0.1 step. For each value of α, data were generated for a total acquisition time of 2000 s and then cropped in order to obtain data sets of length 10, 20, 200, 500, 1000 and 2000 s. The frequency range over which the FD fit is performed was optimally defined by visual inspection separately for each data set. Finally, we considered three noise settings for the simulated strain curves: One where no noise is added, one where the standard deviation of the noise is 1/10-th the standard deviation of the simulated strain, and one where the standard deviation of the noise is 1/2-th the standard deviation of the simulated strain. For each processing technique (Fourier domain (FD) or time domain (TD) fit) and noise level (0,1/10-th and 1/2-th) we then plot the output value of each of the KVFD parameter (α_{out},E_0,τ') versus the input value of α_{in}. This section presents and analyzes the results observed.

4.1.1 Influence on α

Fig. 4.1 presents the output value of α (α_{out}) obtained from the Fourier domain fitting of the data versus the input value of α (α_{in}) for various levels of noise. Without noise, the algorithm appears to perform better when the value of α_{in} is low. As α_{in} increases, the experimental curves deviate

from the ideal relationship between the input and output value of α ($\alpha_{out} = \alpha_{in}$). The maximum deviation appears for the smallest acquisition time and is close to 26% of the input value. Because the FD fit is performed in the log-log space, values at high frequencies tend to have more weight in the linear fit than values at low frequencies. Here, the frequency range over which the fit is performed might be slightly too large and encompass some of the noisy values we observe at high frequency. This noise might be sufficient to overestimate already large slopes, but not smaller ones.

We also notice that as the acquisition time increases, the experimental relationship between α_{in} and α_{out} becomes closer to the ideal relationship. Indeed, as will be confirmed in the next sections, the FD algorithm performs significantly better as the total data acquisition time increases. Large acquisition times mean more points within the frequency range over which the data can be fit, hence more accuracy.

As shown by Fig. 4.2, this is not the case for the time domain processing. In that case, the accuracy appears to be globally better when the total acquisition time is smaller and α_{in} is large. Indeed, up to $\alpha_{in} = 0.4$, the output values of α generally present large deviations. Though this is counter intuitive, we believe this is due to the numerical estimation of the Mittag-Leiffler function in the curve-fitting program based on [40]. Moreover, the time fitting algorithm is non-linear and might be affected by the large number of data samples. Finally, the program is initialized at the values obtained from the FD fit to limit the computation time. Hence, the time domain fit might be affected by the deviation present in the FD fit output as α_{in} increased. This could explain why the largest acquisition time gives globally better results than those observed for 200 to 1000 s. In any case, the processing time for this technique is considerably increased.We therefore reserve this algorithm for very small data sets.

Finally, for both algorithms, as the noise increases in the data, the accuracy on the parameter value decreases. This could be expected, and justifies the use of a spatially averaging window to decrease the level of noise in the creep curves.

4.1.2 Influence on E_0

As can be seen in Fig. 4.3, the output value of E_0 given by the Fourier domain fit gets closer to 10 Pa (its input value) as α_{in} increases. The value of E_0 is estimated for the Fourier domain fit according to $\sigma_0/\epsilon_{total\ acquisition\ time}$, assuming that $\epsilon_{total\ acquisition\ time} \rightarrow \epsilon_\infty$. Hence, as the acquisition time increases, this approximation, as well as the estimated value of E_0, become more accurate. We showed earlier at short times that when α is small, the material creeps faster but also

less than when α is large. At infinity however, the amplitude of the creep does not depend on α. Hence, when we estimate E_0 as being $1/\epsilon(2000)$ in this case, we tend to overestimate it when α_{in} is small. As α_{in} increases, the estimation gets closer to the input value and the algorithm's accuracy increases.

The estimated values of E_0 obtained from the time domain fit (see Fig. 4.4) appear more erratic, probably because of the influence of the initialization and of the estimated value of α_{out}, which tends to be wrong for large acquisition times. It can however be noticed that better results are observed for short acquisition times and large values of α_{in}, which is the typical setting for which this processing technique is used.

As could be expected, the presence of noise decreases the overall accuracy of the algorithms. Though we did not consider it here, one way to decrease the influence of the noise on the estimation of E_0 may be to consider the average value of the amplitude of the creep at the largest available times and not only one value. The choice of the averaging window however becomes an issue and we might underestimate the creep once again by averaging over a time period too long.

4.1.3 Influence on τ'

As can be seen in Fig. 4.5, the output value of τ' gets closer to 2 s (its input value) as α_{in} increases. The value of τ' extracted from the FD fit is correlated with the values of E_0 and α_{out}. We showed earlier that when α_{in} is low, E_0 tends to be overestimated. Hence, the value of τ' compensates for this effect and its output value is lower than its input value when α_{in} is low. As α_{in} increases, the algorithm becomes more accurate regarding E_0 and consequently regarding τ'. When the acquisition time is too short, the value of α_{out} becomes less accurate. Hence, the values of τ' obtained from the FD fit also tend to be less accurate.

Similar trends can be observed with the time domain fit in Fig. 4.6. This proves that the initialization of the TD fit by the FD fit estimation affects this processing technique. The estimates of α and E_0 obtained from the TD fit for short acquisition times and large values of α_{in} were however very accurate, which explains why the performances of the TD fit are good when α_{in} is above 0.6 both for the shortest and longest acquisition times.

To conclude, it has been seen in this section that for large total acquisition times (above 1000 s) and for values of α_{in} typically above 0.6, the FD algorithm leads to very little error in the estimation of each of the KVFD parameter, even with the largest level of noise. Similarly, the TD fit leads to better performances when α_{in} is above 0.6 but for short acquisition times. These settings correspond

to the experimental ones for which these algorithms are respectively used.

4.2 Effects of changes in the fitting frequency range

For this section, we again generated creep curves according to Eq. 2.20. Similarly as in the previous sections, the values of E_0 and τ' were fixed, respectively, at 10 Pa and 2 s and the data sampling rate was 10Hz. Curves were generated for values of α going from 0.1 to 0.9 by an 0.1 step. For each value of α, data were generated for a total acquisition time of 2000 s and then fit in the Fourier domain. Four different frequency ranges were used to fit the data in the Fourier domain: $[0.01-0.1]$, $[0.05-0.5]$, $[0.1-1]$ and $[0.5-5]$ rad.s^{-1}. Finally, the level of noise was adjusted, as in the previous section, for each data set. We again considered three cases: One where there is no noise, one where the standard deviation of the noise is 1/10-th the standard deviation of the simulated data, and one where the standard deviation of the noise is 1/4-th the standard deviation of the simulated data.

As in the previous section, for each level of noise (0,1/10-th and 1/4-th) we then plot the output value of each of the KVFD parameter (α_{out},E_0,τ') versus the input value of α (α_{in}) for each frequency range. This section presents and analyzes the results observed.

4.2.1 Influence on α

As can be seen in Fig. 4.7, the relationship between α_{in} and α_{out} is never ideal. However, a well-chosen frequency range, such as $[0.05-0.5]$ rad.s^{-1}, may lead the output value of α to be closer to the input value. When the frequency range is too low or too high, the output value of α strongly deviates from the input value. Once again, we see that as the noise in the simulated time domain data increases, the algorithm's accuracy decreases.

4.2.2 Influence on E_0

As can be seen in Fig. 4.8, the output value of E_0 gets closer to 10 Pa (its input value) as α_{in} increases. As presented earlier, the value of E_0 is estimated for the FD fit according to $\sigma_0/\epsilon_{total\ acquisition\ time}$. The frequency range chosen for the fit therefore doesn't affect the value of E_0. We however previously showed that the value of α_{in} as well as the level of noise influence the accuracy of the output value of E_0. This is confirmed by Fig. 4.8.

4.2.3 Influence on τ'

As shown previously and pictured in Fig. 4.9, the output value of τ' gets closer to 2 s (its input value) as α_{in} increases since the estimation of E_0, and consequently τ', becomes more accurate. When the fitting frequency range is too high (starting at $[0.1 - 1]$ rad.s^{-1} here), the accuracy on α_{out}, hence on τ', decreases.

To conclude, for a frequency range similar to the one we used ([0.03 to 0.3] rad.s^{-1} for simulation data and [0.1 to 0.6] rad.s^{-1} for experimental phantom or tissue data), and for values of α_{in} similar to those observed in hydropolymers (typically above 0.6 in both phantoms and breast tissues), the FD algorithm leads to very little error in the estimation of each of the KVFD parameter, even with the largest level of noise.

4.3 Global comparison of the two processing techniques

We simulated strain curves with various acquisition times and sampling period and performed on them both the Fourier and time domain fits. We measured the time needed to perform each fit and the mean squared error between the original data and those generated according to the fit parameters. This gave us, for each processing technique, an estimate of its computational cost and performances under various conditions. This may help decide what processing technique is the most appropriate for a considered data set. Fig. 4.10 and 4.11 show the resulting normalized accuracy over processing time ratios for the Fourier and time domain processing, as well as the difference between them. When the difference is positive, the Fourier domain processing has a better accuracy/cost ratio than the time domain processing, while a negative value implies the opposite. For any strain data sets, a simple mapping on this grid presents the best choice in terms of processing technique.

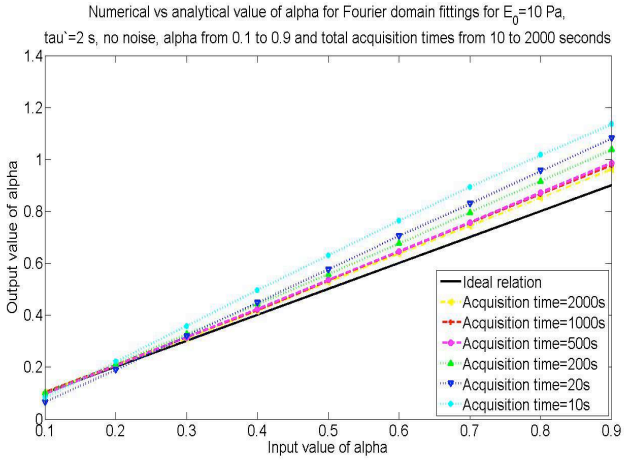

(a)

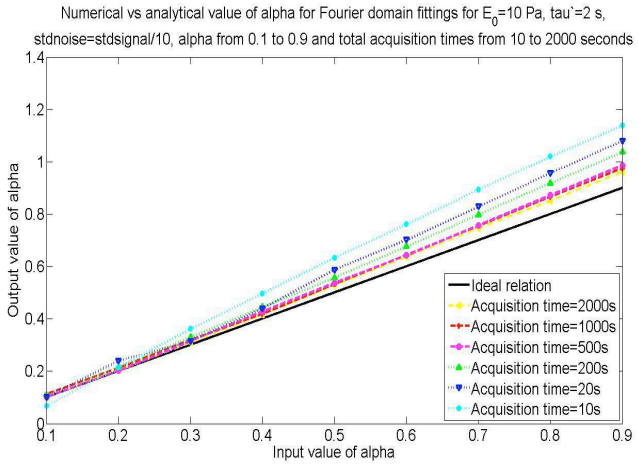

(b)

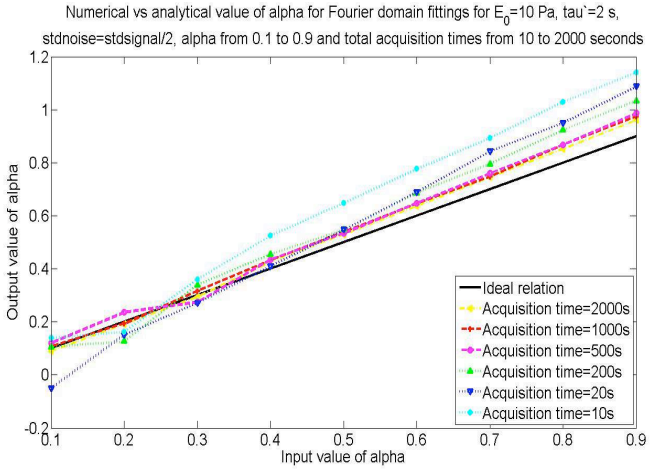

(c)

Figure 4.1: Output vs input value of α given by the Fourier domain fit for different total acquisition times and levels of noise. In a), no noise is added to the simulated strain curves and the best overall performances of the FD algorithm are observed when the acquisition time is the largest. We can see that when the acquisition time is too small the accuracy of the algorithm decreases, especially for high values of α_{in}, which is what can be expected in gelatin or breast tissue samples. In b) and c) we can see that as the noise increases, the global accuracy decreases.

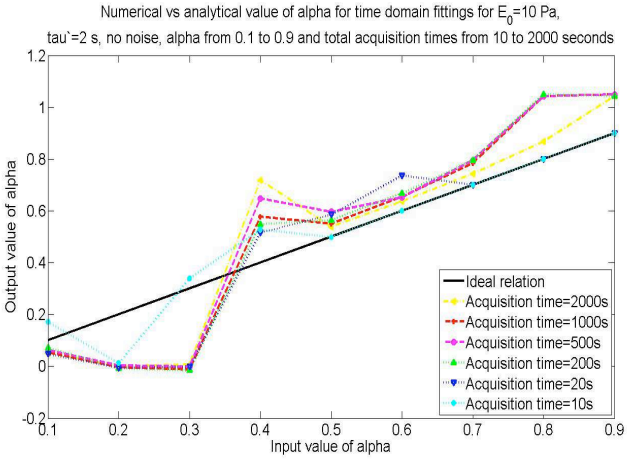

(a)

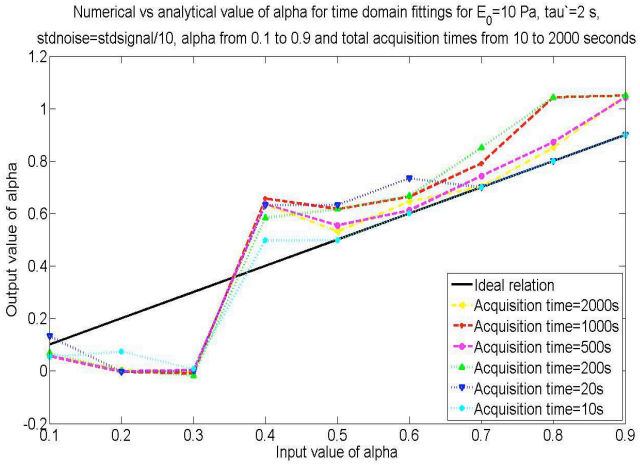

(b)

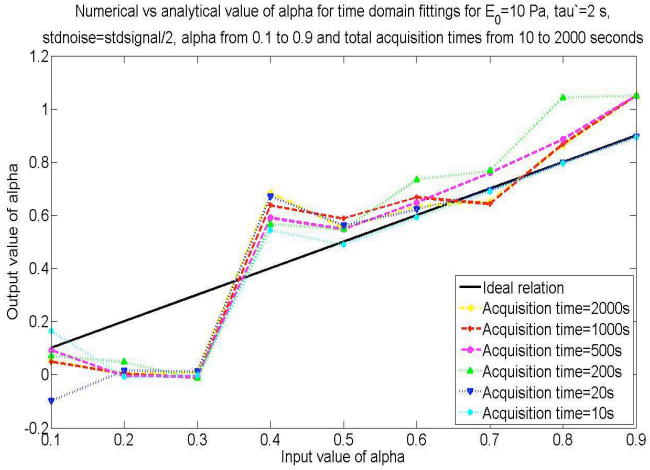

(c)

Figure 4.2: Output vs input value of α given by the time domain fit for different total acquisition times and levels of noise. In a), no noise is added to the simulated strain curves and the best performances of the time domain algorithm are observed when the acquisition time is the smallest. We can see that as the acquisition time increases, the accuracy of the algorithm decreases, with the exception of the case where the acquisition time is 2000 s. This may be due to the non-linearity of the algorithm and to its initialization with the Fourier domain fit output values. In b) and c) we can see that as the noise increases, the global accuracy decreases.

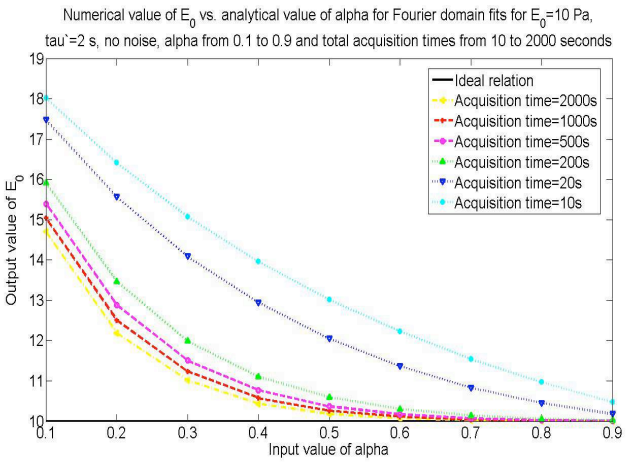

(a)

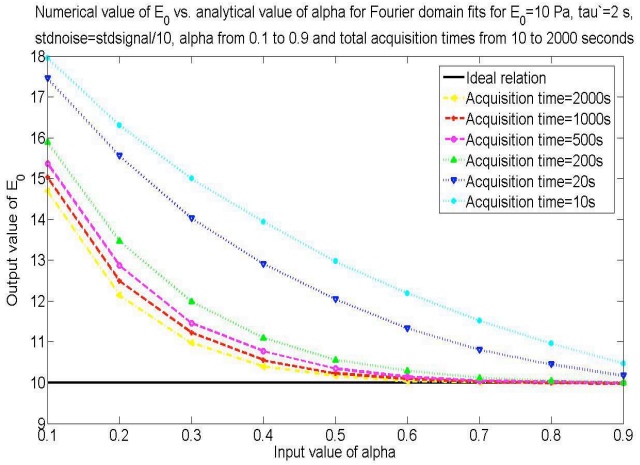

(b)

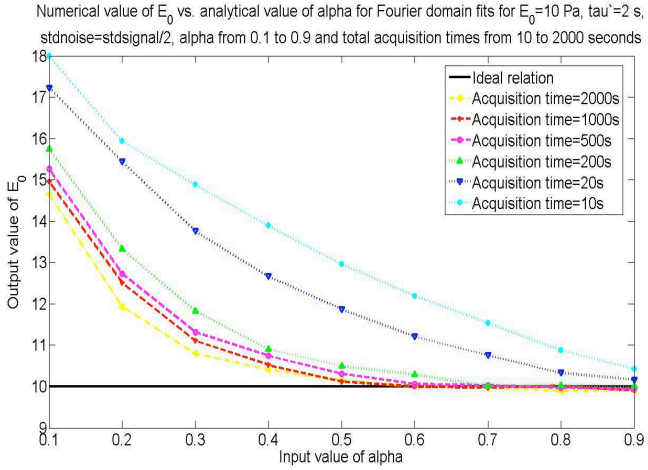

(c)

Figure 4.3: Output value of E_0 given by the Fourier domain fit vs input value of α for different total acquisition time and levels of noise. In a), no noise is added to the simulated strain curves and the performances of the FD algorithm improve both as the acquisition time and α_{in} increase. Indeed, the initial value of E_0 given to the fit is proportional to the inverse of the creep amplitude at infinity, estimated here as the amplitude at the largest available time. As the total acquisition time increases, this approximation, hence the estimation of E_0, become more accurate. In b) and c) we can see that as the noise increases, the accuracy slightly decreases.

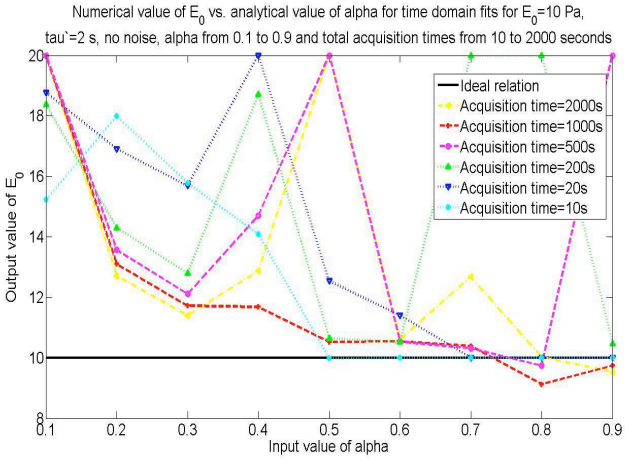

(a)

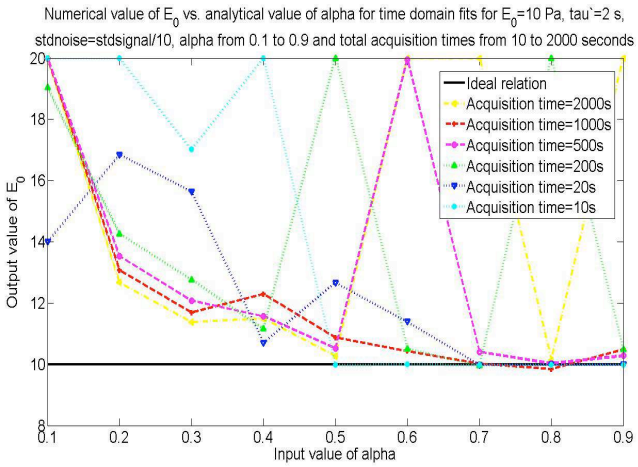

(b)

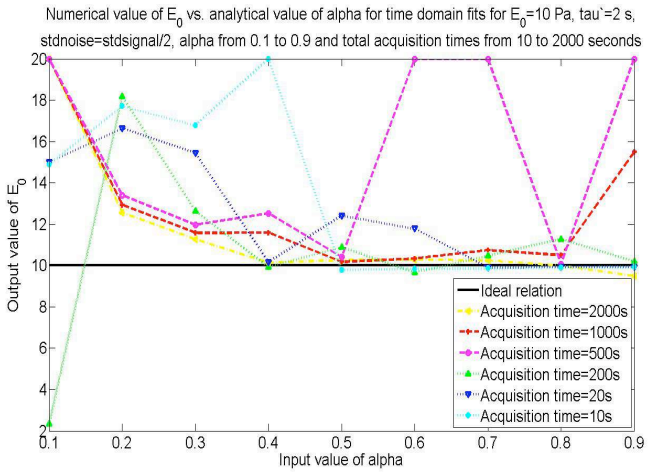

(c)

Figure 4.4: Output value of E_0 given by the time domain fit vs input value of α for different total acquisition time and levels of noise. In a), no noise is added to the simulated strain curves and the performances of the time domain algorithm appear slightly erratic. For the display, we limited the estimated value of E_0 to 20 Pa, i.e. twice its input value. As for the FD fit, the estimation accuracy seems to improve as α_{in} increases, but the best results are on the contrary observed for short total acquisition times. In b) and c) we can see that as the noise increases, the global accuracy decreases and the estimation performances become even more versatile.

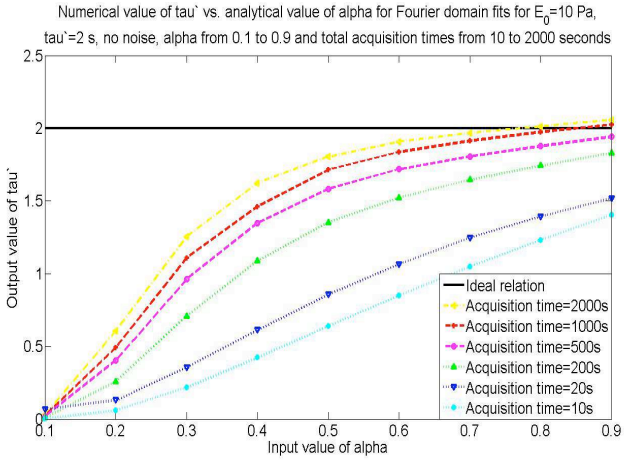

(a)

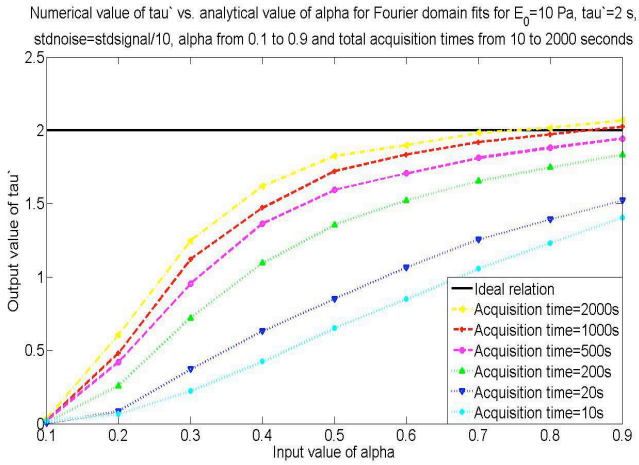

(b)

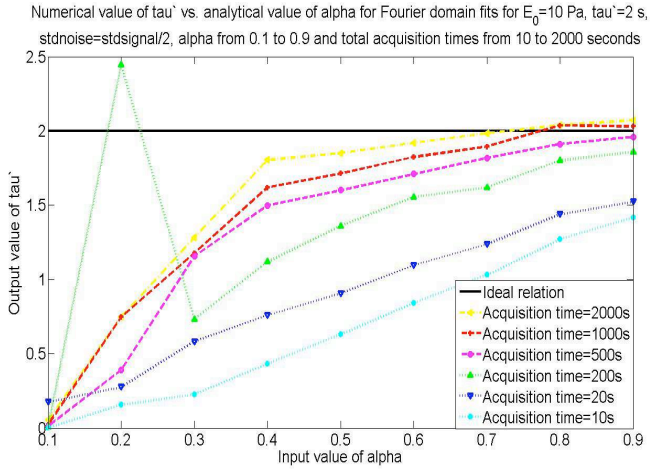

(c)

Figure 4.5: Output value of τ' given by the Fourier domain fit vs input value of α for different acquisition times and levels of noise. In a), we once again notice that when no noise is added, the performances of the algorithm improve as the acquisition time and α_{in} increase. This is due to the correlation between the values of E_0 and τ' given by the fit. In b) and c) we can see again that as the noise increases, the global accuracy decreases though the algorithm seems less affected by the noise when α_{in} is large.

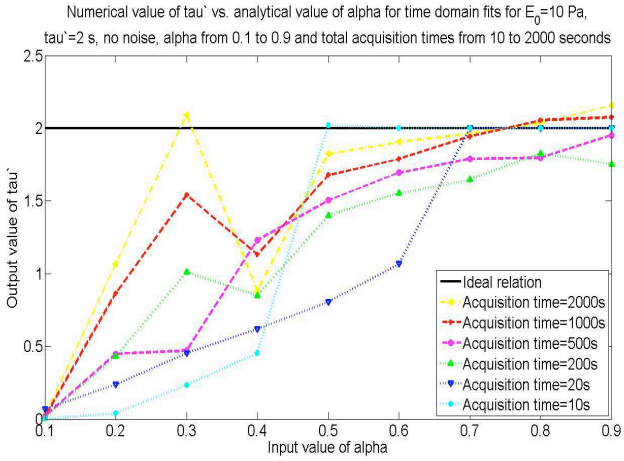

(a)

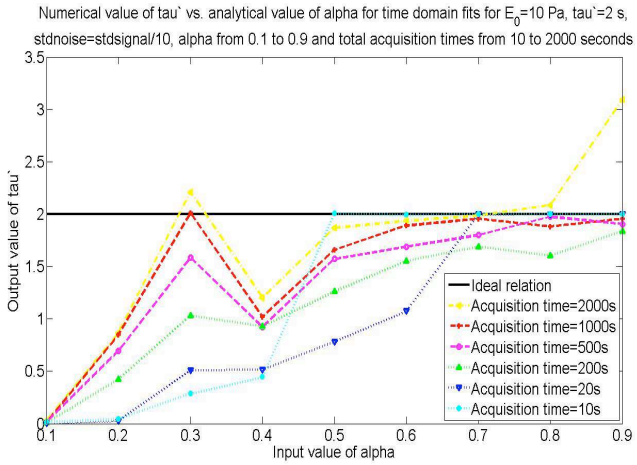

(b)

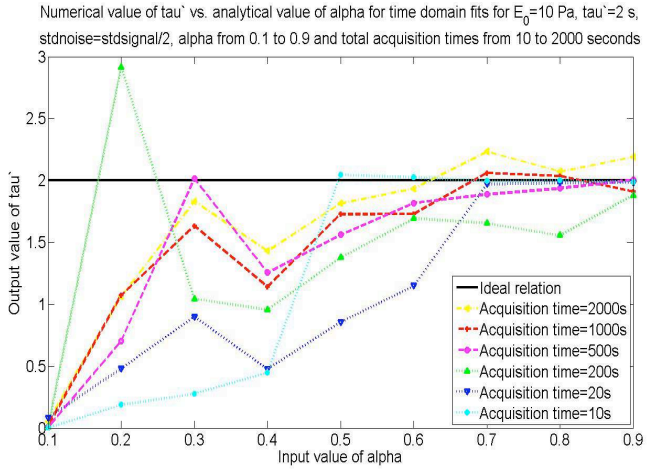

(c)

Figure 4.6: Output value of τ' given by the time domain fit vs input value of α for different acquisition times and levels of noise. In a), b) and c), we notice that for any level of noise, the overall performances tend to increase as α_{in} increases. The corresponding performances are the best when the acquisition time is the smallest, though the largest acquisition times also lead to high accuracy. This is most likely due to the initialization by the FD fit, which performs better for larger acquisition times.

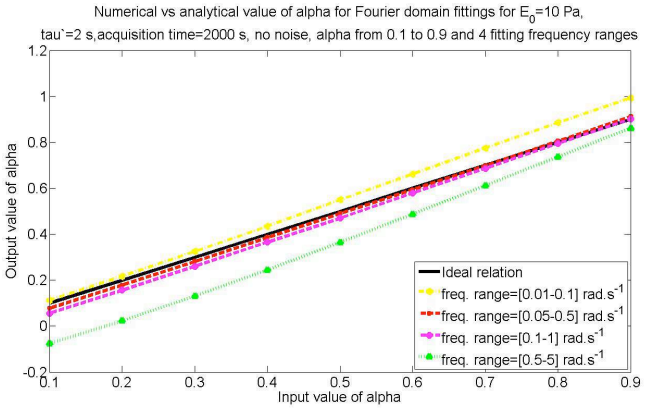

(a)

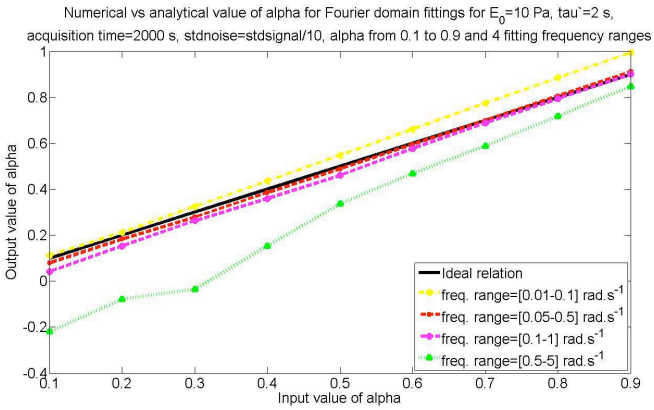

(b)

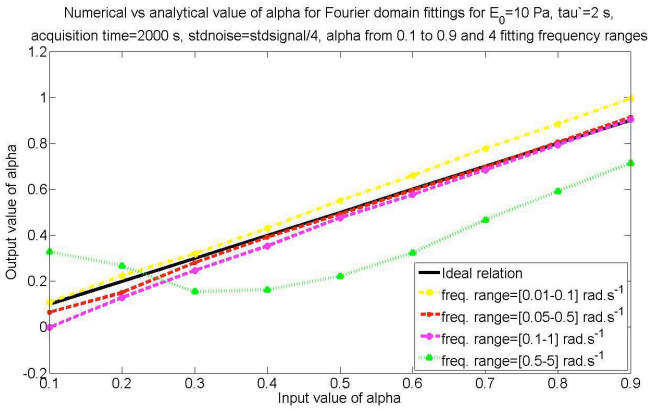

(c)

Figure 4.7: Output vs input value of α for different fitting frequency ranges and levels of noise. In a), no noise is added to the simulated strain curves and the best performances of the FD algorithm are observed when the fitting frequency range is $[0.05 - 0.5]$ rad.s^{-1} which is the closest to the frequency range used for experimental data. We can see that when the frequency range is too low, or, worse, too large, the accuracy of the algorithm decreases. In b) and c) we can see that as the noise increases, the global accuracy decreases. However, when the fitting range is better chosen, the fit seems less affected than when it is too extreme, as illustrated by the results for the $[0.5 - 5]$ rad.s^{-1} frequency range.

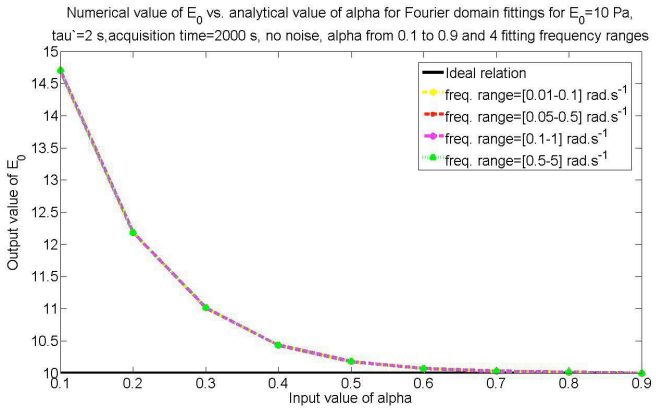

(a)

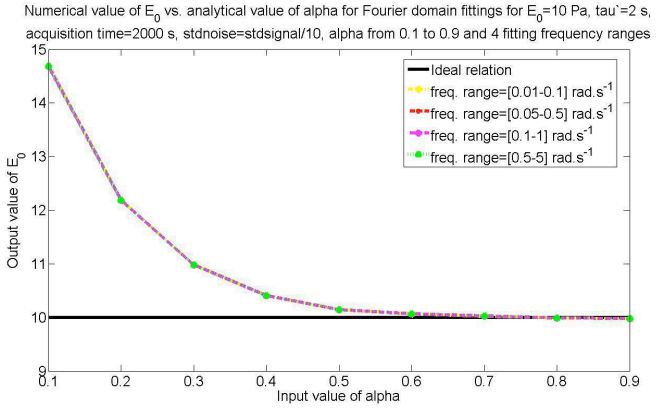

(b)

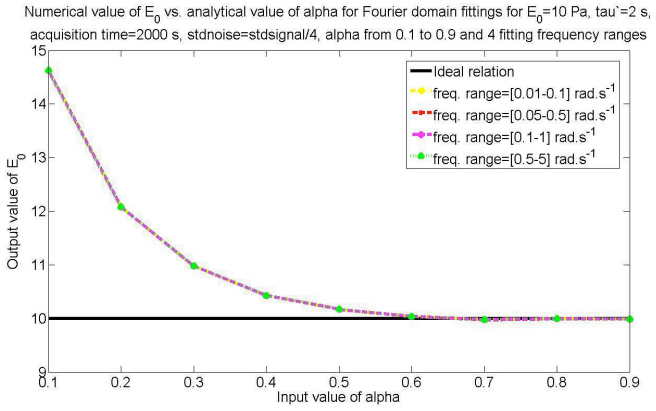

(c)

Figure 4.8: Output value of E_0 vs input value of α for different fitting frequency ranges and levels of noise. In a), no noise is added to the simulated strain curves and the performances of the FD algorithm are similar for all the frequency ranges. Indeed, the initial value of E_0 given to the fit is proportional to the inverse of the creep amplitude at infinity, which doesn't change. The accuracy however increases with α_{in}. Indeed, we previously noticed at short times that when α is low, the material strains less but quickly. Hence, when we assume the creep amplitude at infinity to be the creep amplitude at 2000 s, we underestimate $\sigma_0/E_0 = 1/E_0$ here. The lower the input value of α, the more overestimated the output value of E_0. As α increases, the initial estimation of E_0 improves and tends to the input value. In b) and c) we can see that as the noise increases, the accuracy slightly decreases.

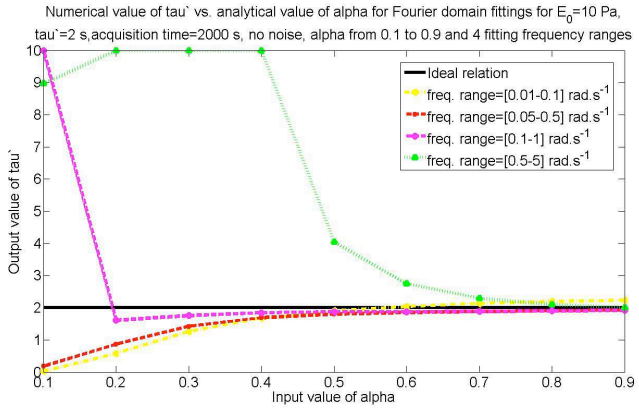

(a)

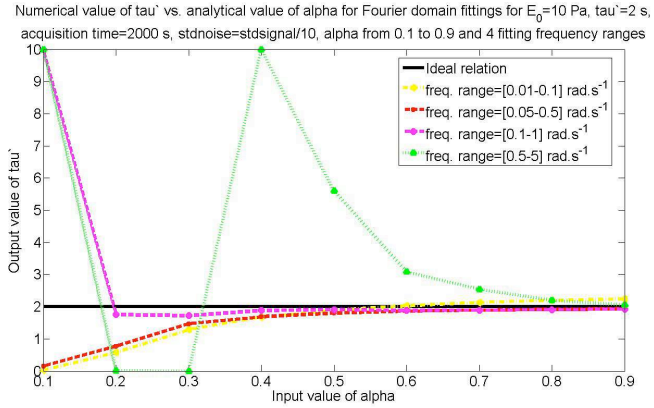

(b)

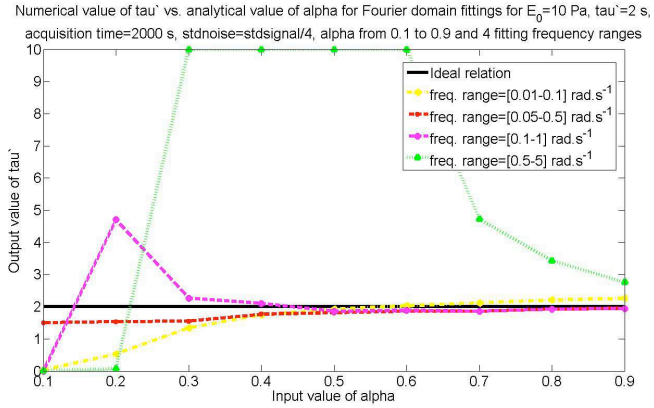

(c)

Figure 4.9: Output value of τ' vs input value of α for different fitting frequency ranges and levels of noise. In a), we once again notice that when no noise is added, the overall performances of each frequency range are similar, though the highest frequency range gives poor results when α_{in} is low. We also notice that the accuracy increases as α increases. This is due to the correlation between the values of E_0 and τ' given by the fit. We previously showed that when α is low, E_0 is overestimated. In compensation, τ' is underestimated. As α_{in} increases, the values of E_0 and α_{out} get more accurate, and so does the value of τ'. In b) and c) we can see again that as the noise increases, the global accuracy decreases though the algorithm seems less affected by the noise when the frequency range is relatively low ($[0.05 - 0.5]$ rad.s^{-1}) than when the frequency range is high ($[0.5 - 5]$ rad.s^{-1}). (Notice that we restricted the values of τ' to $[0; 10]$ s for this display but some of the values obtained were originally higher)

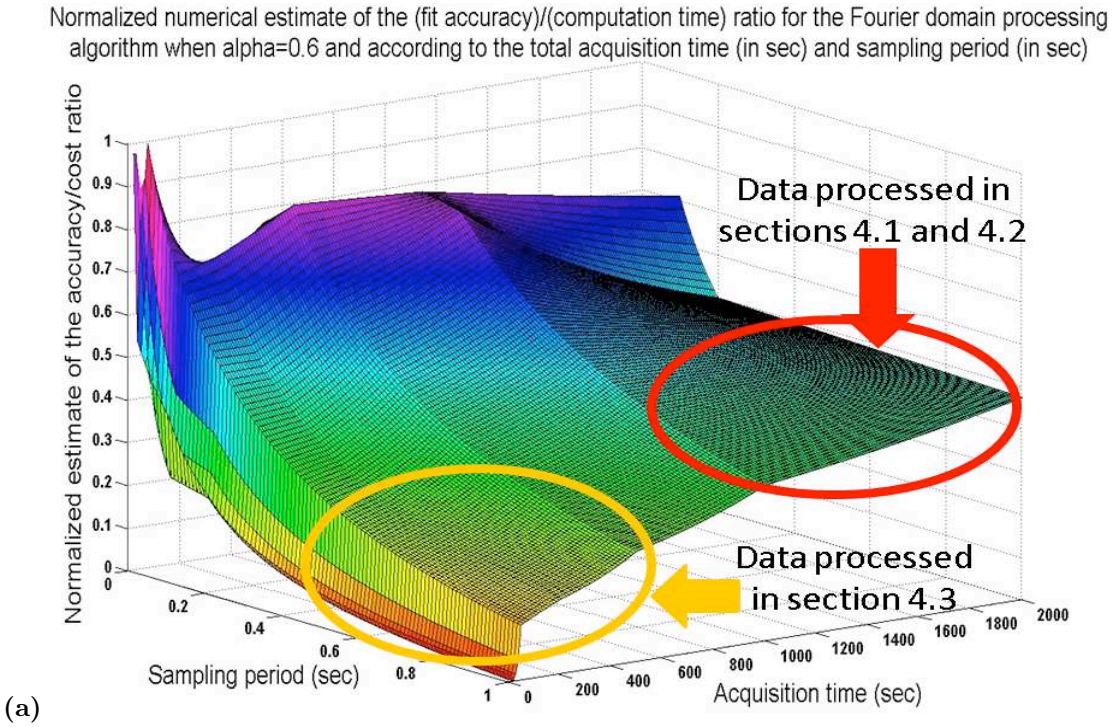

(a)

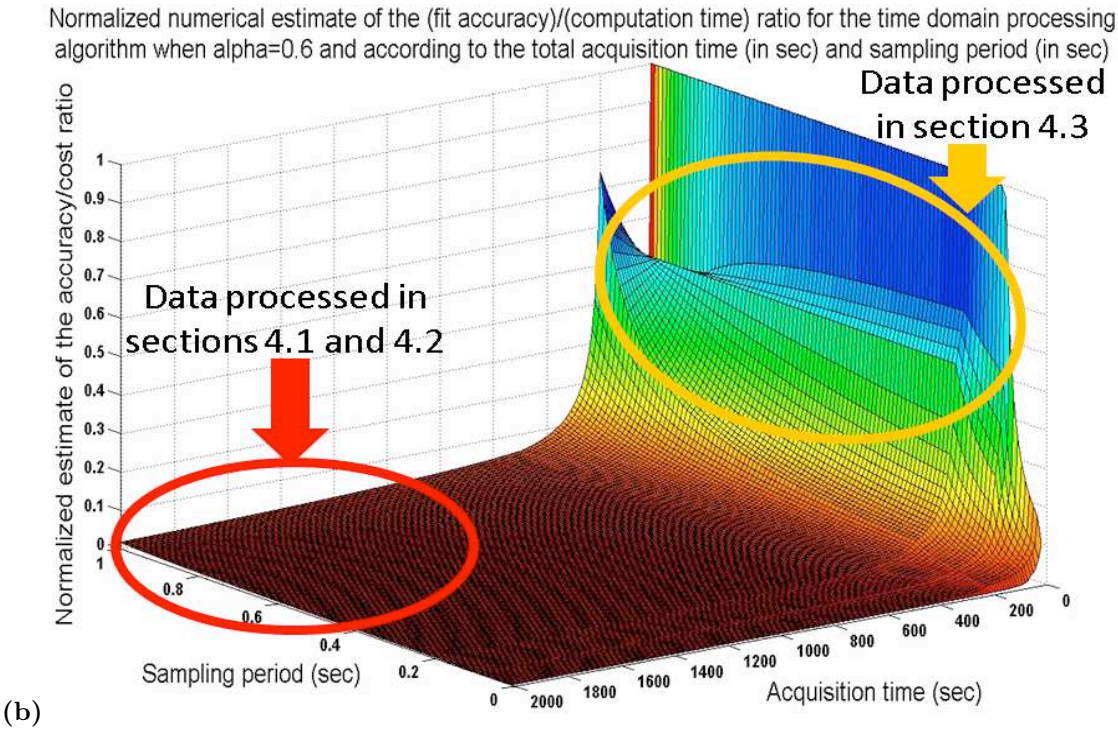

(b)

Figure 4.10: Quality/price ratios for the Fourier and time domain processing algorithms according to the strain data acquisition time and sampling period. It can be seen in a) that it is more interesting to use the Fourier domain processing when the acquisition time is large, and the sampling period relatively low. However, its quality/price ratio is very low when the acquisition time is low. On the other hand, the corresponding graph in b) confirms that the time domain processing performs relatively better when used on data with short acquisition times and any sampling period.

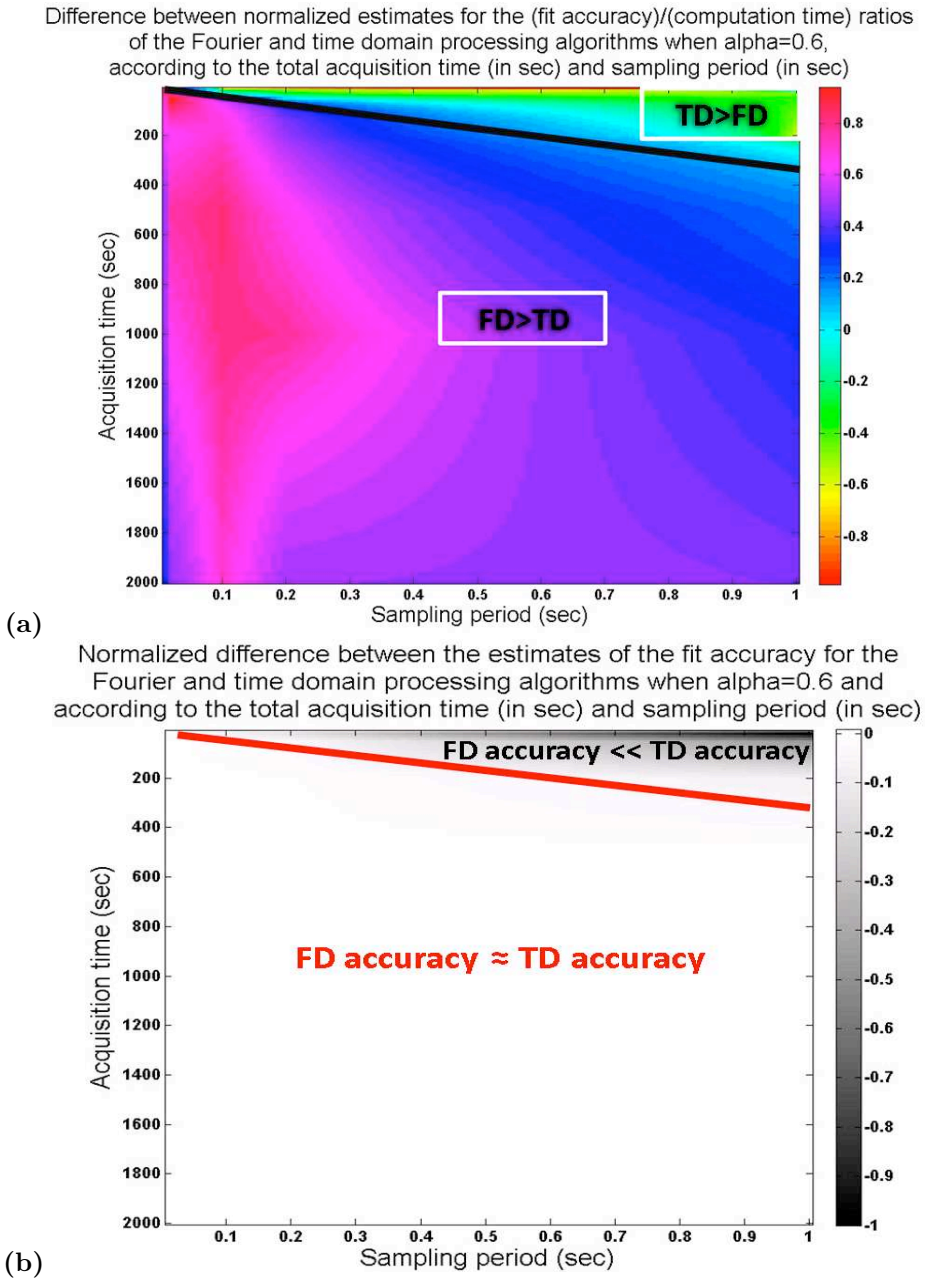

Figure 4.11: Comparison of the Fourier and Time domain algorithms performances. a) shows the difference of normalized fit accuracies between the Fourier and time domain algorithms. Notice that both algorithms have similar accuracies across most of the acquisition time and sampling period considered. However, the Time domain algorithm is much more reliable when the acquisition time of the data is short and the sampling period large, i.e. when we have very little data. In b) is displayed the difference between the quality/price ratios of the Fourier and time domain processing algorithms according to the strain data acquisition time and sampling period. As hinted by Fig. 4.10, the difference is positive, meaning that it is better to use the Fourier domain processing, when the acquisition time of the data is large. However, the difference is negative, meaning that it is wiser to use the time domain processing, when the acquisition time of the data is small. Here, b) is intended to show that though the lower computational cost of the Fourier domain algorithm might lead to higher quality/price ratio with very low accuracy values, it is not the case here and the TD fit is indeed reliable when the acquisition time is long enoughfig422.

Chapter 5

Results

Here, we present and analyze the α, E_0 and τ' parameters values and images for simulated and experimental phantoms as well as in-vivo breast tissue data.

5.1 Stiff inclusion image simulations

Two different software phantoms simulations are conducted in this section. Our primary goal here is to generate two phantoms according to well-known and well interpretable physical characteristics (such as the permeability k or Poisson's ratio ν_m), to image the corresponding KVFD parameters and to analyze and correlate them with the physical input parameters. The second goal was to prove that materials could be differentiated based on their KVFD parameter values.

For each simulation, a stiff circular inclusion is positioned in a soft background material. Viscoelastic model parameters for these two simulations are listed in Table 5.1. In the first simulation, the phantom is made such that its inclusion reacts to the applied force as a material stiffer than its background. The inclusion indeed presents a higher elastic modulus, E_m, and a large permeability constant, k, to allow for fast fluidic motion. The solid matrix's relaxation time constants are also lower in the inclusion to allow for a quick viscoelastic response. In the second simulation, the inclusion's elastic modulus, E_m, is also higher than in the background. However, the other parameters responsible for the viscoelastic response of the phantom, such as the Poisson's ratio, permeability, or characteristic time constants, are similar inside and outside the inclusion. This means that the second phantom presents different initial elastic responses in the inclusion and background but similar viscoelastic responses.

From the FEA presented in section 3.2., we generate displacement maps for each phantom as a function of time. FEA displacement fields are processed to generate object strains and the object parametric images observed in Fig. 5.1. These maps are also used to model the displacements of random scattering fields and RF waveforms are generated to simulate echo signals from a linear

array. The ultrasonic parametric images obtained from these RF echo simulations are shown in Fig. 5.2. The average KVFD parameters estimated from the images presented in Fig. 5.1 and 5.2 are listed in Table 5.2. The object strain images present very little noise and could be immediately processed. However, the simulated RF echo images in themselves presented a relatively high level of noise, that was amplified by the MRCC processing needed to obtain the ultrasonic strain frames sequence. A companding window of 256 pixels was used, and the resulting strain images were post-processed with both an averaging and median filters to decrease the level of noise in the creep curves.

These strain image sequences were then processed by our algorithm in order to extract the KVFD parameters. For the object strain data, a spatially averaging window of only 3x3 pixels was used, while the processing of the ultrasonic data required the use of a 27x49 pixels averaging window, as depicted in Fig. 3.1. The KVFD parameter images, as well as a typical strain image extracted from the strain sequence after post-processing when necessary, are respectively presented in Fig. 5.1 and 5.2.

As expected from the simulation's input parameters, the object and ultrasonic strain image sequences present a significantly lower strain ϵ in the inclusion. The initial elastic response being mostly linked to the elastic modulus E_m and to the Poisson's ratio ν_m of the solid matrix, this is no surprise. Because of the inverse proportional relation between the amplitude of the creep and the KVFD parameter E_0, the E_0 images for both simulations present higher values in the center.

With no further inspection, one may conclude that both phantoms have similar properties. Indeed, their strain images look almost identical and present similar values across time. Looking at the KVFD parameter images however provides more information on the viscoelastic properties of these two phantoms and uncovers the differences between them.

In the first simulation and for both types of processing the α images (Figs. 5.1 and 5.2) present significantly lower values in the inclusion, which indicates a stiffer, more elastic material and is consistent with the simulation's input. Indeed, as stated earlier, the amplitude of the creep is lower in this region and the time constants smaller which is typical of elastic materials and modeled with low values of α. In the second simulation however, very little contrast can be observed on the alpha images, whatever the processing. The average values of α inside and outside the inclusion are similar (see Tables 5.1 and 5.2) and relatively high, which indicates that the inclusion and background in simulation (2) share similar viscoelastic properties and are relatively viscous.

In the second simulation, there is also very little contrast to be observed in the τ' object and

ultrasonic parametric images, though contrast magnitude is reduced in the later. In the first simulation however, the τ' images change depending on the processing. For the object strain sequence, τ' is lower in the inclusion, which indicates a fast fluidic motion as hinted by the simulation's viscoelastic parameters. The contrast is however inverted in the ultrasonic parametric image. The values observed in the background are similar to those observed with the object data, but the values observed in the inclusion are higher. We attribute this artefact to the FD processing technique. Indeed, as stated earlier, the estimated values of E_0, τ' and α are correlated. The spatially averaging window needed to process the data here is much larger for the ultrasonic data than for the object data. This means that strain curves from the inclusion have been averaged with strain curves in the background, causing an increase of the creep amplitude. This is most likely responsible for the lower values of E_0 that can be observed in the inclusion for the ultrasonic data. Hence, τ' increases in order to compensate for the decrease of E_0 in order to fit the data correctly. This might also explain why the values of α observed in the ultrasonic data are slightly different from those observed with the object data.

Our first goal here was to show that the KVFD parameter values were linked to physical parameters of the material and could describe its viscoelastic characteristics with very few features and images. Our second objective was to show that phantoms, or more generally regions, could be differentiated only based on their KVFD parameter images. Processing the object as well as the ultrasonic data enabled us to achieve both of these goals and showed that the viscoelastic characteristics of simulated hydropolymers may be represented with only three parameters. The next section will show that similar results may be extracted from the experimental study of hydropolymers.

E_m (Pa)	Inclusion	13500	13500
	Background	4500	4500
ν_m	Inclusion	0.45	0.47
	Background	0.47	0.47
k ($\mathrm{m.s^{-1}}$)	Inclusion	50×10^{-11}	25×10^{-11}
	Background	5×10^{-11}	25×10^{-11}
g_1, τ_1(s)	Inclusion	0.02, 1	0.02, 5
g_2, τ_2(s)		0.04, 5	0.04, 25
	Background	0.08, 20	0.06, 5
		0.16, 100	0.12, 25

Table 5.1: FEA simulation parameters for the two simulations. For both phantoms the initial elastic response indicates that the inclusion is stiffer than the background. In the second simulation, the viscoelastic properties of the inclusion and background, modeled by k, ν_m and the time constants τ_1 and τ_2, are similar. This is not the case in the first simulation, where these parameters differ.

Object parametric images			
	Simulation #	(1)	(2)
α	Inclusion	0.621 ± 0.002	0.810 ± 0.002
	Background	0.959 ± 0.002	0.813 ± 0.001
E_0	Inclusion	1221 ± 1	1564 ± 2
(Pa)	Background	261 ± 2	378 ± 2
τ'	Inclusion	21 ± 1	15 ± 1
(sec)	Background	63 ± 2	18 ± 1
ϵ_0	Inclusion	0.70	0.72
(%)	Background	1.22	1.32
ϵ_∞	Inclusion	0.78	0.79
(%)	Background	1.61	1.61
Ultrasonic parametric images			
	Simulation #	(1)	(2)
α	Inclusion	0.49 ± 0.01	0.95 ± 0.02
	Background	0.89 ± 0.02	0.93 ± 0.04
E_0	Inclusion	458 ± 6	544 ± 5
(Pa)	Background	265 ± 2	350 ± 4
τ'	Inclusion	150 ± 12	16.4 ± 0.1
(sec)	Background	67 ± 2	19.8 ± 0.3
ϵ_0	Inclusion	0.65	0.73
(%)	Background	1.21	1.31
ϵ_∞	Inclusion	0.81	0.82
(%)	Background	1.59	1.60

Table 5.2: Average KVFD model parameter values (α, E_0 and τ') estimated in the inclusion and background for the object (top) and ultrasonic (bottom) parametric images displayed in Fig. 5.1 and 5.2.

5.2 Gelatin phantoms

5.2.1 Higher concentration inclusion phantom

A gelatin phantom with a high concentration of gelatin in the inclusion (8% by weight as opposed to 5.5% in the background) was built according to the technique presented in section 3.3.1 and processed according to the method described in section 3.1.2. Because of the high level of noise present in the strain data, we had to post-process the data with both an averaging and median filter which significantly smoothed the strain curves and frames. This allowed us to obtain the KVFD parameters at each one of the strain image's pixel with a spatially averaging window of 17x17 pixels. These parameter images are presented in Fig. 5.3.

As could be expected, the strain image extracted from the strain frame sequence indicates that the inclusion strains less than the background. Indeed, it has been previously observed that a high concentration of gelatin stiffens the phantom. This explains the significantly higher elastic modulus

E_0 observed in this parameter image. The α parameter image presents lower values in the inclusion, which confirms its higher stiffness. Finally, the values of τ' are higher in the inclusion, which may indicate a fluidic motion slower in the inclusion than in the background. Indeed, the inclusion contains more gelatin molecules that might trap and retain the water molecules. In that case, a longer time may be needed for water to move. However, the processing artefact observed in the first simulation of the previous section might also be responsible for this contrast.

Indeed, simulation (1) in the previous chapter was intended to show characteristics similar to those observed in this experiment. We can therefore compare the contrasts observed in the KVFD parameters for purely simulated data (Fig. 5.1), for simulated RF echo frames processed with the MRCC algorithm (Fig. 5.2) and finally for purely experimental data (Fig. 5.3). The trends observed in the strain frames, E_0 and α images are similar, and the values of α observed in the experimental case are within the range of these observed in the simulation. The values of τ' are however slightly higher than what could be expected, while the values of E_0 are lower than in the simulation. This tends to show that the processing artefact does affect the data, though both the gelatin concentration and processing technique might affect the value of τ' here.

These results suggest that the KVFD model parameters may be used to concisely represent the main VE properties of not only simulated but also experimental phantoms.

Parameter	Inclusion	Background
α	0.60 ± 0.04	0.76 ± 0.01
E_0	246 ± 2	140 ± 1
τ'	83 ± 10	38 ± 1

Table 5.3: Average KVFD model parameter values (α, E_0 and τ') in the inclusion and background for the experimental phantom presented in section 4.2.1)

5.2.2 Acidic and basic inclusion phantoms

The ultimate goal of this work is to differentiate between benign and malignant tumors based on the KVFD parameter values. Micro-environmental changes are generally associated with a breast tumor's development and may affect the VE properties of these tissues and consequently the KVFD parameter values, allowing the differentiation of the mass. Among these are pH changes.

Two gelatin phantoms (isoelectric pH 5.6) were injected, respectively, with acidic and basic solutions during polymerization according to the technique presented in 3.3.2. These pH changes are thought to affect the gelatin matrix arrangement [41], provoking a softening of the medium

in presence of an acid, and a stiffening with a basic injection. Hence, the strain image sequences obtained for these phantoms with inclusions polymerized at pH 4.6 (Fig. 5.4a) and 6.6 (Fig. 5.4b) show that an acidic fluid injection leads to a softening of the inclusion, while a basic one stiffens the center of the phantom.

An experimental artefact linked to the injection causes a bright central region to appear in the strain images for both phantoms (see Yapp [41]). Moreover, a relatively high noise is present in the data, which prevented us from displaying the KVFD parameter images. For some regions however, the level of noise was lower and we display in Fig. 5.4 the average KVFD parameter values in regions located inside and outside the inclusion for both phantoms.

These confirm what was previously observed. Indeed, E_0 is lower in the acidic inclusion and higher in the basic one, which is consistent with the strain values observed in both cases. The study of α confirms the matrix changes following the inclusion. Indeed, the average value of α is lower in the basic than in the acidic inclusion, which indicates that it is more elastic than the background gelatin at its isoelectric point (pH= 5.6) or at pH= 4.6. The values of τ' suggest that water moves more rapidly in the basic than in the acidic inclusion, which may be due to the higher number of charges present in the later as observed by Yapp [41].

Though only pH changes were considered here, several modifications appear within a tumor's micro-environment during its development. These might induce changes in the viscoelastic properties of the tumor and tumor area. These results show that the KVFD parameter images may reflect such environmental changes around a tumor mass, hence providing clues to differentiate between tumor types.

5.3 In-Vivo breast tissue data study

In chapter 3, we compared the performance vs cost ratios of the Fourier and time domain processing techniques for various experimental parameters. We showed that for total acquisition times lower than 200 s, the use of the time domain fit is recommended. For the previous simulations and experiments, the total acquisition times were between 1800 and 5000 s. We had largely enough data to use the Fourier domain processing, hence to quickly obtain reliable KVFD parameters estimates. However, in this section, the data were acquired over less than 180 seconds. We therefore performed a time domain fit to the KVFD model.

5.3.1 Average gelatin phantom and breast tissue responses

Previously, we observed the viscoelastic properties of simulated and experimental hydropolymers. In this section, our goal is to compare the KVFD parameter values in gelatin phantoms and in in-vivo normal breast tissue. Because the noise in such experimental data is generally high, we spatially averaged the creep curves obtained for a phantom and tissue region. The resulting two curves were fit, in the time domain, to Eq. (2.20) as shown in Fig. 5.5. For comparison, the Fourier domain fitting algorithm was also used to fit the data to the KVFD model for frequencies ranging from 0.02 to 0.2 rad.s^{-1}. As the reader may see, both fits give similar results.

The corresponding KVFD model parameters appear in Table 5.4. The values of E_0 are significantly lower than these observed previously. However, this might be due to the lack of data. Indeed, E_0 is estimated from ϵ_∞ which is, in this case, estimated from $\epsilon(180)$. The data are therefore most likely too short to estimate E_0, hence to estimate τ' since both parameters' values, estimated from the fits, are correlated.

Though we may not be able to trust the values of E_0 and τ', the values of α are consistent with previous observations [20]. It can indeed be seen that α tends to be higher in breast tissue than in gelatin, which means that breast tissues have a less elastic and more fluidic response than gelatin phantoms. The KVFD parameters may therefore also be able to represent the main viscoelastic characteristics of in-vivo breast tissues.

KVFD model Parameter	Gelatin Phantom		Breast Tissue	
	TD fit	FD fit	TD fit	FD fit
α	0.543	0.536	0.830	0.800
E_0	16.6	14.6	22.9	22.3
τ'	59.3s	54.7s	15.4s	15.2

Table 5.4: KVFD approach parameter values (α, E_0 and τ') obtained from average gelatin and tissue responses. The TD fit corresponds to a time domain fitting of the strain curve to Eq. (2.20), and the FD fit to the fitting of the loss modulus in the Fourier domain to Eq. (2.24). Both processings give similar results, though the Fourier domain fitting is significantly faster.

5.3.2 Cancer patient data

In the previous section, we showed that KVFD parameters could be extracted by a time domain fit from in-vivo breast tissue strain data. The next step would be to image KVFD parameter images for breast tissues and to differentiate tumors. Though we were not able to obtain such results, we present in this section KVFD parameters from several normal and tumorigenic breast tissue regions.

Clinical ultrasonic data were previously obtained for breast cancer patients with non-palpable and biopsy-confirmed benign and malignant tumors [42]. These data were only acquired over 10 to 20 seconds. We therefore used a time domain fit. However, the important level of noise and short acquisition time strongly affect the KVFD model parameters values observed. Indeed, E_0 is initialized at a value inversely proportional to $\epsilon(10)$ which is obviously very different from ϵ_∞. In any case 10 seconds is a little too short to estimate the material's behavior. This considerably affects the values we obtain and the parameter images appear really noisy. Though we therefore cannot use these images to differentiate the types of tumors, we can however get estimates of the typical KVFD model parameter values in breast tissues with more confidence than in the previous section and believe that better parameter images could be extracted for longer data sets.

Table 5.5 shows that τ' values are generally larger in lesions than in the background, and that E_0 values in the benign lesions are much larger than those in the corresponding background regions. Conversely, lesion and background values for E_0 are more similar in malignant tumors. This observation is consistent with the histological view of benign lesions having a solid, elastic nature because of their dense concentration of normal collagen. Non-palpable malignant lesions, on the other hand, retain a more fluidic viscoelastic response even with increases in collagen density because of differences in the ECM proteins. These observations are contradicted by the values of α. For all parameters, more data sets with longer acquisition times are needed to draw any conclusions about diagnostic value.

	Simulation #	(1)	(2)	(3)	(4)	(5)
α	Lesion	0.81 ± 0.03	0.95 ± 0.07	0.89 ± 0.03	0.78 ± 0.02	0.99 ± 0.03
	Background	0.73 ± 0.09	0.86 ± 0.04	0.91 ± 0.05	0.79 ± 0.02	0.820 ± 0.005
E_0	Lesion	88 ± 6	140 ± 5	78 ± 6	51 ± 4	90 ± 8
(Pa)	Background	45 ± 5	50 ± 2	106 ± 4	49 ± 6	28.1 ± 0.6
τ'	Lesion	1.6 ± 0.3	1.5 ± 0.2	2.6 ± 0.4	1.8 ± 0.2	2.23 ± 0.05
(sec)	Background	0.6 ± 0.3	0.7 ± 0.2	1.4 ± 0.04	1.9 ± 0.1	0.87 ± 0.02

Table 5.5: Average KVFD model parameter values (α, E_0 and τ') in the lesion and background of 2 benign and 3 malignant breast tumors.

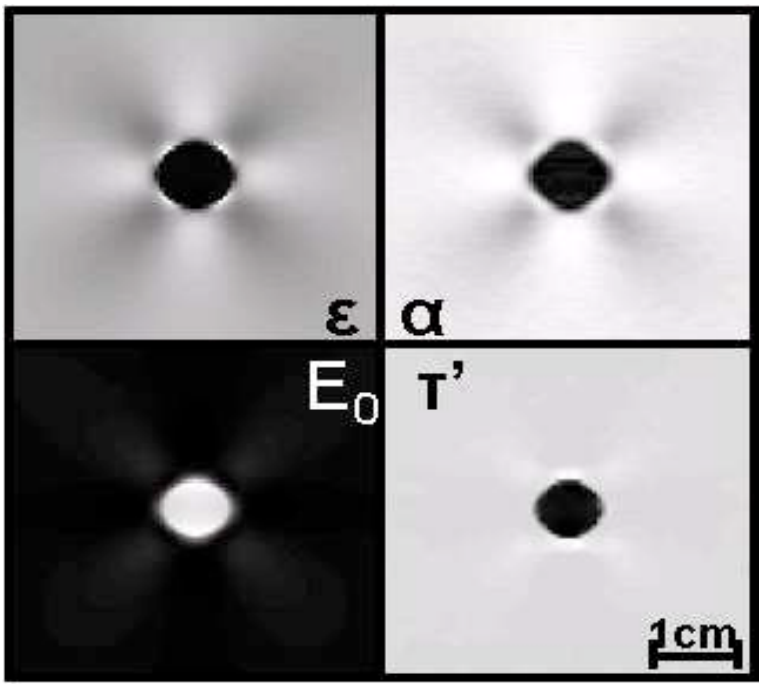

Simulation (1)

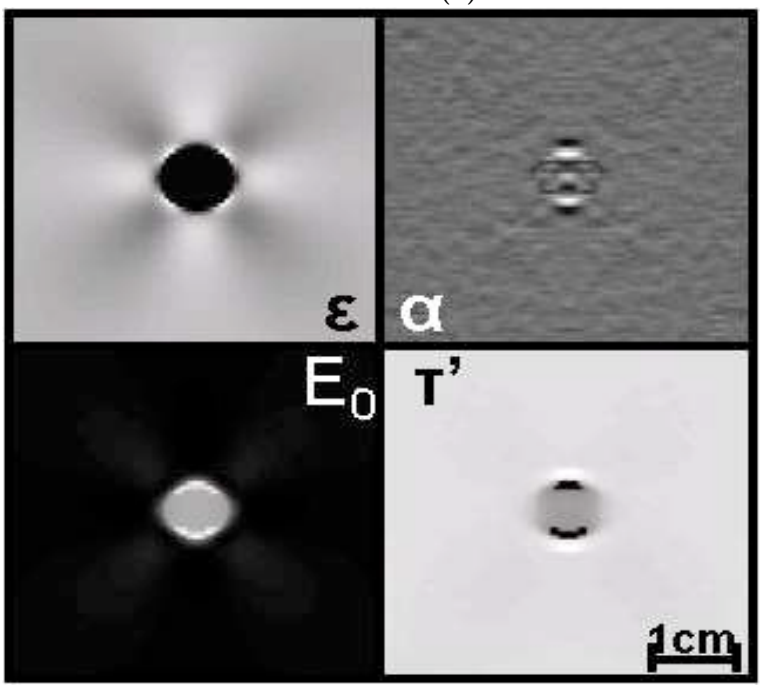

Simulation (2)

Figure 5.1: KVFD model images obtained for the strain image sequences generated from derivation of the interpolated FEA displacements: Object parametric images. Two simulated phantoms with VE properties given in Table 5.1 are compared using the KVFD approach. Elastic strain (ϵ, top left) and elastic modulus (E_0, bottom left) images for both simulations appear similar while the α (top right) and relaxation time (τ', bottom right) images show significant contrast differences in the two simulations. In simulation (1), the α image shows that the inclusion is more elastic and less fluidic than the background, whereas the inclusion and background have similar viscoelastic responses in simulation (2). Lower values of τ' in the inclusion in simulation (1) and not in (2) indicate differences in fluid motion.

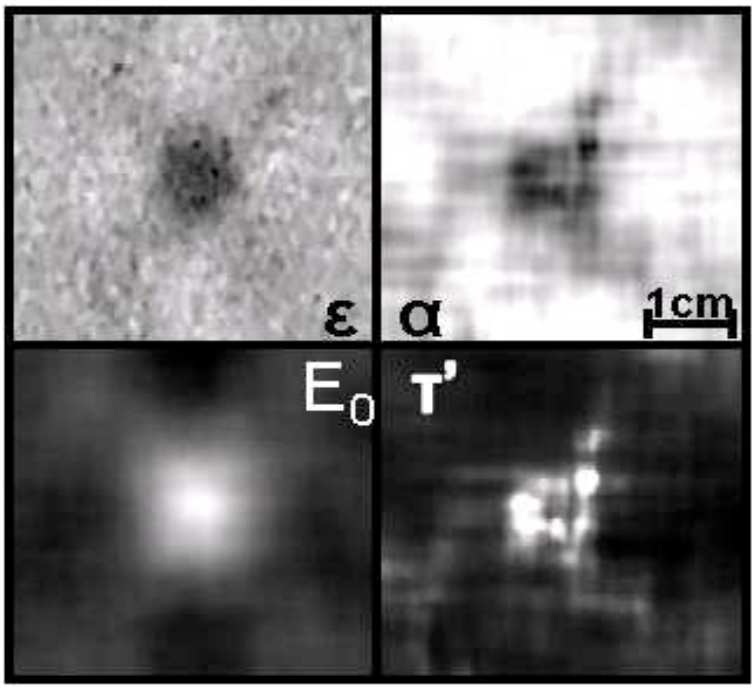

Simulation (1)

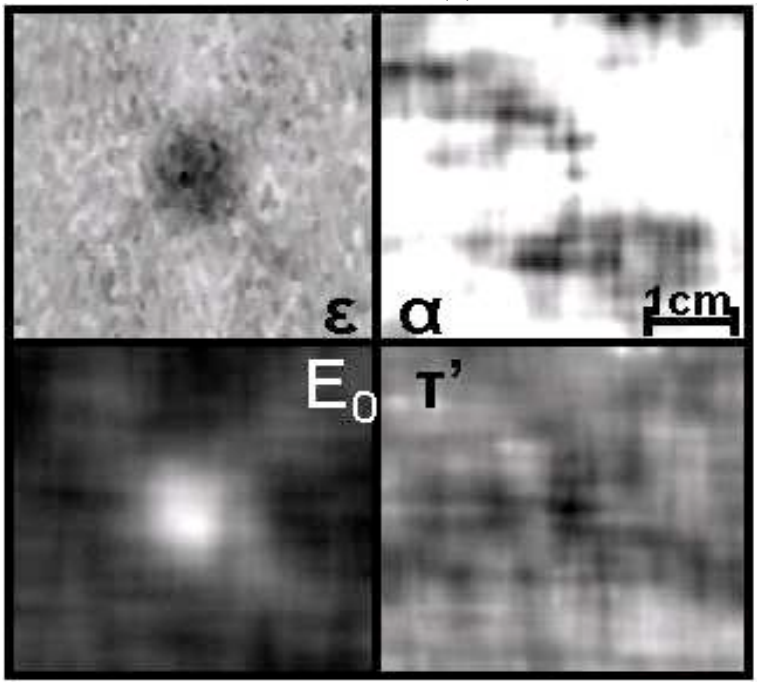

Simulation (2)

Figure 5.2: KVFD model images obtained for the strain image sequences generated from simulated echo data of two deformed FEA phantoms: Ultrasonic parametric images. These images give results similar to those observed in Fig. 5.1. The parameter images show significant contrast in simulation (1) but the inclusion disappears in the α and τ' images from simulation (2). In simulation (1), a processing artefact is responsible for the inverted contrast of the τ' image.

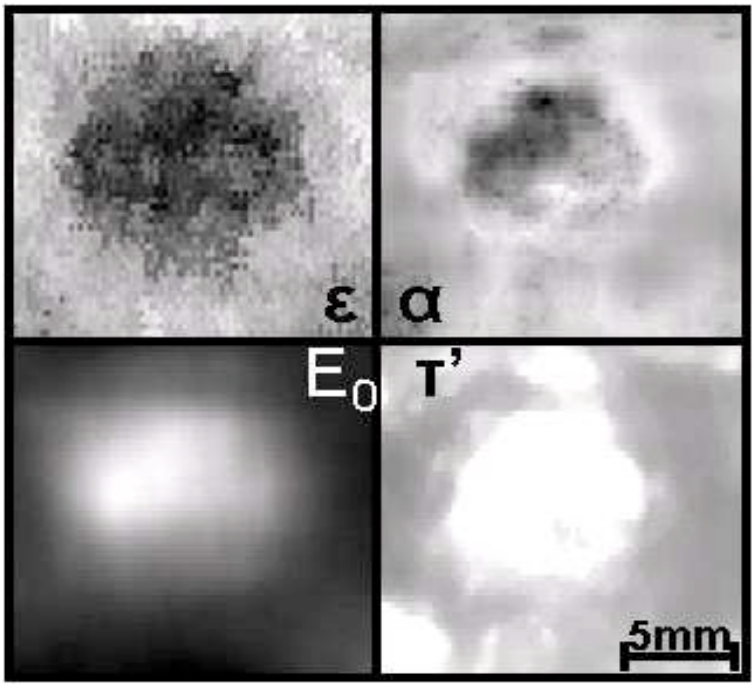

Figure 5.3: KVFD parameter images for an experimental gelatin phantom with a stiff inclusion of diameter 8 mm: The blurring effect is due to the expanded size of the spatially averaging window needed to decrease strain noise. The values observed for E_0 show that the inclusion region creeps less than the background region. The α image displays lower values in the inclusion, which indicates that it is more elastic than the background. The τ' image indicates a slow fluidic response of the center of the polymer, which may be due to its higher concentration of gelatin (trapping water molecules). The average parameter values inside and outside the inclusion are given in table 5.3.

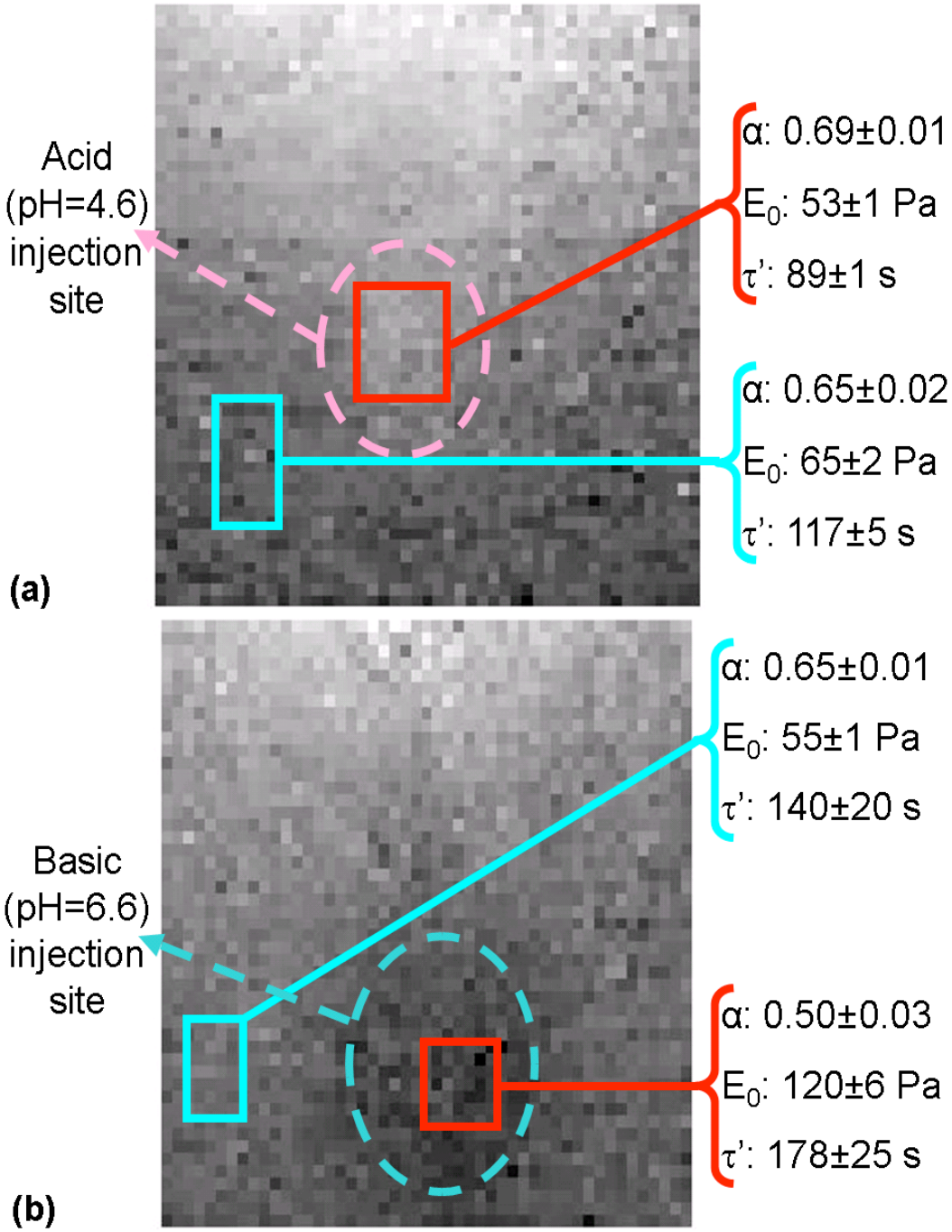

Figure 5.4: Typical strain images obtained for two type-B gels respectively injected in the inclusion with an acidic and basic solution during polymerization and corresponding average KVFD parameter values in two regions. In a), a strain frame of the acidic inclusion phantom is displayed. The inclusion appears brighter, which is consistent with α being higher in the inclusion and indicating a more viscous material. In b), the basic inclusion appears darker in the strain image, which is consistent with the smaller value of α in the inclusion indicating a more elastic region.

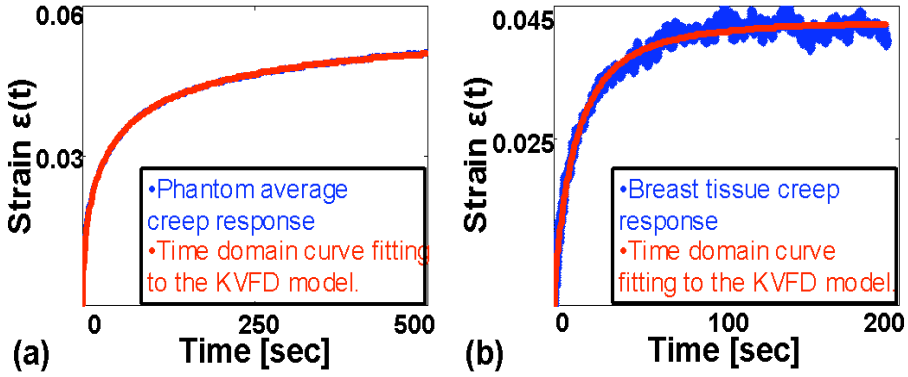

Figure 5.5: Average creep response observed in an experimental phantom (a) and in breast tissue (b) fit in the time domain to Eq (2.20). The corresponding KVFD model parameters are given in Table 5.4.

Chapter 6

Conclusion

In this thesis, we proposed applications of fractional derivatives to rheological modeling in order to reduce the feature space for materials characterization and thus provide parameters for imaging. After mathematically justifying the use of fractional derivatives, we imaged and analyzed the three parameters of the KVFD model for simulated and experimental hydropolymers as well as in-vivo breast tissue data. We showed that regions with significantly different viscoelastic responses are easily detected with this method and may be differentiated provided the data acquisition time is long enough and strain noise is limited. Though we were not able to consistently differentiate non-palpable breast tumors in patient data, we identified typical parameter values and were able to show, based solely on the three parameters of the model, that breast tissues are significantly more viscous than hydropolymers with faster internal fluidic motions than gelatin phantoms. We were also able to differentiate an acidic region from a basic one in gelatin as well as two simulated phantoms, and thus consider a similar technique, with improved image quality, to be very promising for tumor differentiation. However, the correlation between the values of E_0 and τ' derived from the fit and the effect of spatial averaging on these parametric images is an issue that needs to be addressed. Such processing artefact may affect the contrast in parametric images and lead the observer to the wrong conclusion. Though one parameter $\mu = E_0 \tau'^{\alpha}$ may be defined, as in previous studies [31], to represent the combined effects of the three KVFD parameters, the physical analysis of the FD model would become very challenging. Since it has been seen here that the value of α is uncorrelated to the other parameters and mainly unaffected by the spatially averaging window while still retaining a large amount of diagnostic information, future work may focus on the analysis of this parameter.

References

[1] MB Kossoff, Ultrasound of the breast, *World J. Surg.*, vol. 24, pp. 143-57, 2000.

[2] C Marini, C Traino, A Cilotti, M Roncella, G Campori, C Bartolozzi, Differentiation of benign and malignant breast microcalcifications: mammography versus mammography-sonography combination, *Radiol. Med. (Torino)*, vol. 105, pp. 17-26, 2003.

[3] BS Garra, EI Cespedes, J Ophir, SR Spratt, RA Zuurbier, CM Magnant, MF Pennanen, Elastography of breast lesions: initial clinical results, *Radiology 202* pp. 79-86, 1997.

[4] A Thomas, S Kmmel, F Fritzsche, M Warm, B Ebert, B Hamm, T Fischer, Real-time sonoelastography performed in addition to B-mode ultrasound and mammography: improved differentiation of breast lesions? *Acad. Radiol.*, vol. 13, pp. 1496-504, 2006.

[5] A Thomas, M Warm, M Hoopmann, F Diekmann, T Fischer, Tissue Doppler and strain imaging for evaluating tissue elasticity of breast lesions, *Acad. Radiol.*, vol. 14, pp. 522-9, 2007.

[6] H Zhi, B Ou, BM Luo, X Feng, YL Wen, HY Yang, Comparison of ultrasound elastography, mammography, and sonography in the diagnosis of solid breast lesions, *J. Ultrasound Med.* vol. 26, pp. 807-15, 2007.

[7] B Elenbaas, R Weinberg, Heterotypic signaling between epithelial tumor cells and fibroblasts in carcinoma formation, *Exp Cell Res 264*, pp.169-184, 2001.

[8] DE Discher, P Janmey, Y-L Wang, Tissue cells feel and respond to the stiffness of their substrate, *Science*, vol. 310. pp. 1139-43, 2005.

[9] S Suresh, Biomechanics and biophysics of cancer cells, *ACTA Biomaterialia* vol. 3, pp. 413-38, 2007.

[10] JF Greenleaf, M Fatemi, M Insana. Selected methods for imaging elastic properties of biological tissues, *Annual Review of Biomedical Engineering*, vol. 5, Martin Yarmush, ed. Annual Reviews: Palo Alto pp. 57-78, 2003.

[11] P Chaturvedi, M F Insana, T J Hall, 2-D companding for noise reduction in strain imaging, *IEEE Trans. Ultrason. Ferroelectr. Freq. Control*, vol. 45, pp. 179-91, 1998.

[12] C Pellot-Barakat, F Frouin,M F Insana, A Herment, Ultrasound elastography based on multiscale estimations of displacement regularized fields, *IEEE Trans. Med. Imaging* vol. 23, pp. 153-63, 2004.

[13] F Viola, WF Walker, A spline-based algorithm for continuous time-delay estimation using sampled data, *IEEE Trans. Ultrason. Ferroelectr. Freq. Control*, vol. 52, pp. 80-93, 2005.

[14] GF Pinton, GE Trahey, Continuous delay estimation with polynomial splines, *IEEE Trans. Ultrason. Ferroelectr. Freq. Control*, vol. 53, pp. 2026-35, 2006.

[15] KR Nightingale, ML Palmeri, RW Nightingale, GE Trahey, On the feasibility of remote palpation using acoustic radiation force, *J. Acoust. Soc. Am.* vol. 110, pp. 625-34, 2001.

[16] M Sridhar,J Liu, M F Insana, Elasticity imaging of polymeric media, *ASME J. Biomechan. Eng.*, vol. 129, pp.259-72, 2007.

[17] A F Mark, The apparent viscoelastic behavior of articular cartilage: The contributions from the intrinsic matrix viscoelasticity and interstitual fluid flows, *ASME J. Biomechan. Eng.*, vol. 108, pp. 123-130, 1986.

[18] A F Mark, Unconfined compression of hydrated viscoelastic tissues: A biphasic poroviscoelastic model, *Biorheology*, vol. 23, pp. 371-383, 1986.

[19] M R DiSilvestro, J K Suh, Biphasic poroviscoelastic behavior of hydrated biological soft tissue, *ASME J. Appl. Mech.*, vol. 66, pp. 528-535, 1999.

[20] M Sridhar, M F Insana, Ultrasonic measurements of breast viscoelasticity, *Med. Phys.*, vol. 34, pp. 4757-67, 2007.

[21] H Muir, Proteoglycans as organizers of the intercellular matrix, *Biochem. Soc. Trans.*, vol. 11, pp. 613-22, 1983.

[22] JD Ferry, *Viscoelastic Properties of Polymers*, Wiley, New York, 1980.

[23] M Sridhar, J Liu, M F Insana, Viscoelasticity imaging using ultrasound: parameters and error analysis, *Phys. Med. Biol.*, vol. 52, pp. 2425-43, 2007.

[24] R L Bagley, P J Torvik A theoretical basis for the application of fractional calculus to viscoelasticity, *Journal of Rheology*, vol. 27, pp. 201-10, 1983.

[25] M Z Kiss, T Varghese, T J Hall, Viscoelastic characterization of in vitro canine tissue, *Phys. Med.Biol. 49*, pp.4207-18, 2004.

[26] V D Djordjevic, J Jaric, B Fabry, J J Fredberg, D Stamenovic, Fractional derivatives embody essential features of cell rheological behavior, *Ann. Biomed. Eng.*, vol. 11, pp. 692-7, 2003.

[27] D Y Song, T Q Jiang, Study on the constitutive equation with fractional derivative for the viscoelastic fluids - Modified Jeffreys model and its application, *Rheol. Acta* vol. 37, pp. 512-17, 1998.

[28] N Heymans, Fractional calculus description of nonlinear viscoelastic behavior of polymers, *Nonlinear Dynamics*, vol. 38, pp. 221-31, 2004.

[29] GL Sloninsky, Laws of mechanical relaxation processes in polymers, *J. Polym. Sci.; Part C*, vol. 16, pp. 1667-72, 1967.

[30] H Schiessel,A Blumen, Hierarchical analogues to fractional relaxation equations, *J. Phys. A:Math. Gen.*, vol. 26, pp. 5057-69, 1993.

[31] H Liu, T E Oliphant, L Taylor, General fractional derivative viscoelastic models applied to vibration elastography, *IEEE Ultrason. Symp.*, pp. 933-6, 2003.

[32] A Chatterjee, Statistical origins of fractional derivatives in viscoelasticity, *J. Sound Vibr.* vol. 284, pp. 1239-45, 2005.

[33] T Pfitzenreiter, A physical basis for fractional derivatives in constitutive equations, *ZAMM: Z. Angew. Math. Mech.* vol. 84, pp.284-7, 2004.

[34] Y Kawada, H Nagahama, H Hara, Irreversible thermodynamic and viscoelastic model for power-law relaxation and attenuation of rocks, *Tectonophysics* vol. 427, pp. 255-63, 2006.

[35] Y Kawada, H Nagahama, Viscoelastic behaviour and temporal fractal properties of lherzolite and marble: possible extrapolation from experimental results to the geological time-scale, *Terra Nova*, vol. 16, pp. 128-32, 2004.

[36] H Schiessel, R Metzler, A Blumen, T F Nonnenmacher, Generalized viscoelastic models: their fractional equations with solutions, *J. Phys. A:Math. Gen.* vol. 28, pp. 6567-84, 1995.

[37] M G Mittag-Leffler, Sur la nouvelle fonction $E_\alpha(x)$, *Comptes Rendus Acad. Sci. Paris*, vol. 137, pp. 554-8, 1903.

[38] N W Tschoegl, *The Phenomenological Theory of Linear Viscoelastic Behavior,* Springer-Verlag, Berlin, 1989.

[39] J Liu, CK Abbey, MF Insana, Linear approach to axial resolution in elasticity imaging, *IEEE Trans. Ultrason. Ferro. Freq. Control*, vol. 51, pp. 716-25, 2004.

[40] S W J Welch, R A L Ropper and R G Duren Jr., Application of time-based fractional calculus methods to viscoelastic creep and stress relaxation of materials, *Mech. Time-Dependent Mater. 3*, pp. 279303, 1999.

[41] R D Yapp, S Kalyanam, M F Insana, Molecular and structural analysis of viscoelastic properties,*Proc SPIE*, vol. 6511, pp. 1Y1-11, 2007.

[42] M F Insana, C Pellot-Barakat, M Sridhar, K Lindfors, Viscoelastic imaging of breast tumor microenvironment with ultrasound, *J. Mammary Gland Biol., Neoplasia, 9*, pp.393-404, 2004.

Author's Biography

Cecile Coussot received her B.S degree in engineering from Supelec, France, in 2006 and is currently working towards her M.S in Bioengineering at the University of Illinois at Urbana Champaign. She presented her work at the 2007 IEEE International Ultrasonics Symposium and is the recipient of one of the 2007 Roy S Carver fellowships. Her research interests include modeling and analyzing polymer and breast tissue viscoelasticity. After the completion of her M.S., she will go back to France and work as a consultant for so@t.